A Quadrature-Based Kinetic Model for Dilute Non-Isothermal Granular Flows

Alberto Passalacqua[1,*], Janine E. Galvin[2], Prakash Vedula[3], Christine M. Hrenya[4] and Rodney O. Fox[1]

[1] *Department of Chemical and Biological Engineering, Iowa State University, Ames, IA 50011-2230, USA.*

[2] *United States Department of Energy National Energy Technology Laboratory, Morgantown, WV 26507-0880, USA.*

[3] *School of Aerospace and Mechanical Engineering, University of Oklahoma, Norman, OK 73019-0601, USA.*

[4] *Department of Chemical and Biological Engineering, University of Colorado, Boulder, CO 80309-0424, USA.*

Abstract. A moment method with closures based on Gaussian quadrature formulas is proposed to solve the Boltzmann kinetic equation with a hard-sphere collision kernel for mono-dispersed particles. Different orders of accuracy in terms of the moments of the velocity distribution function are considered, accounting for moments up to seventh order. Quadrature-based closures for four different models for inelastic collision-the Bhatnagar-Gross-Krook, ES-BGK, the Maxwell model for hard-sphere collisions, and the full Boltzmann hard-sphere collision integral-are derived and compared. The approach is validated studying a dilute non-isothermal granular flow of inelastic particles between two stationary Maxwellian walls. Results obtained from the kinetic models are compared with the predictions of molecular dynamics (MD) simulations of a nearly equivalent system with *finite-size* particles. The influence of the number of quadrature nodes used to approximate the velocity distribution function on the accuracy of the predictions is assessed. Results for constitutive quantities such as the stress tensor and the heat flux are provided, and show the capability of the quadrature-based approach to predict them in agreement with the MD simulations under dilute conditions.

---

*Corresponding author. *Email addresses:* `albertop@iastate.edu` (A. Passalacqua), `janine.galvin@netl.doe.gov` (J. E. Galvin), `pvedula@ou.edu` (P. Vedula), `hrenya@colorado.edu` (C. M. Hrenya), `rofox@iastate.edu` (R. O. Fox)

1 Introduction

The behavior of a granular flow can be described by the Boltzmann-Enskog kinetic equation [4,14,35], in terms of the velocity distribution function. Depending on the value of the Knudsen number of the flow, defined as the ratio between the molecular mean free path and a characteristic length scale of the system under consideration, it is often possible to find a simplified set of equations to describe the flow [4,12,13,35]. In particular, when the Knudsen number is zero, a granular flow of elastic particles behaves as an inviscid flow and can be described by the Euler equation. When the Knudsen number is between zero and 0.01, the Navier-Stokes-Fourier (NSF) equations, computed with no-slip boundary condition, represent a simplified set of equations, derived considering the lower-order moments of the kinetic equation. When the Knudsen number is between 0.01 and 0.1, the NSF equations require the introduction of partial-slip boundary conditions to account for rarefaction effects due to the presence of a significant Knudsen layer near the walls. For even larger Knudsen numbers, higher-order solutions of the Boltzmann-Enskog kinetic equation are required to obtain satisfactory results, since the rarefaction effects extend from the walls to the bulk of the fluid, and cannot be treated with the simple modification of the boundary conditions.

Different strategies have been developed to find solutions of the kinetic equation. A possible strategy is to directly discretize the seven-dimensional phase space [2,11], in order to reconstruct the velocity distribution function. However, the high dimensionality of the equation often makes the direct approach impractical due to its high computational cost. An alternative approach to solve the kinetic equation is given by discrete methods, where the trajectory of the particles and their interactions are tracked. In particular, the Direct Simulation Monte Carlo (DSMC) method [4], which relies on notional particles and a statistical description of their interaction, has been widely applied in rarefied gas dynamics to obtain solutions of the kinetic equation for point particles (Boltzmann equation). Molecular dynamics (MD) has been used to compute granular flows of finite-size[†] particles [23], providing solutions of the complete Boltzmann-Enskog kinetic equation. These approaches are efficient for systems with a relatively low number of particles (order of millions), but become intractable for systems of larger scale, related to industrial applications of granular flows and fluid-particle flows.

An interesting and more computationally efficient approach for complex flows is represented by the method of moments, where the idea of reconstructing the velocity distribution is usually abandoned in favor of tracking the spatial and temporal evolution of a finite set of its moments. Moment methods have been widely studied in the literature and a good summary can be found in [35]. The main difficulties in moment methods are

---

[†]With *finite-size particles* we indicate particles that are *not* assumed to be points. Finite-size particles cannot overlap, as it happens with point particles. In the framework of kinetic theory, *point particles* are described by the Boltzmann collision integral, while finite-size particles are described by the Boltzmann-Enskog collision integral. In terms of the moment equations, the point-particle approximation neglects the contribution due to the collisional fluxes.

providing closures for the moment transport equations and formulating boundary conditions for the high-order moments. An alternative approach using partial reconstruction of the velocity distribution is the quadrature method of moments (QMOM), originally developed to deal with population balance equations [31, 33, 38], and recently extended to deal with kinetic equations [15, 21] and the Boltzmann equation [18, 19]. In QMOM, the source terms and the moment spatial fluxes in the moment transport equations are closed using Gaussian quadrature formulas. The velocity distribution function is reconstructed from the moments as a set of Dirac delta function, uniquely defined by a quadrature inversion algorithm [18, 19], which allows the set of transported moments to be correlated with a unique set of quadrature weights and abscissas.

The objective of this work is to construct quadrature-based closures for a bounded conductive system, constituted by a non-isothermal granular flow between two walls at different temperatures, using a kinetic description with four different collision models (BGK [3], ES-BGK [28], Maxwell model [32] and complete Boltzmann). The QMOM results are validated against molecular dynamics (MD) simulations [23]. The elasticity properties of the particles are described by a restitution coefficient, whose value varies between 0.90 and 1, and particle volume fractions set to 0.025 and 0.05, corresponding to Knudsen numbers of 0.191 and 0.095, respectively. Quadrature-based moment methods of third-, fifth- and seventh-order, obtained by increasing the number of quadrature nodes from 8 to 27 and 64 respectively, are considered.

The remainder of this work is organized as follows. In Section 2 the Boltzmann kinetic equation is introduced, the moment transport equations are presented, and the four models for the collision term are described. Further details concerning the derivation of the collision models are given in the appendices. In Section 3 the quadrature-based moment method is discussed and the expressions for the quadrature-based closure of the moment fluxes and collision terms are reported. In Section 4 the solution algorithm for the moment transport equations is briefly reviewed. Section 5 describes the conductive bounded system under examination, and introduces the statistical quantities used to compare the QMOM and MD simulations. Results obtained with the proposed method are presented and discussed in Section 6, and conclusions are drawn in Section 7.

2   Moment methods for the Boltzmann kinetic equation

The kinetic equation describing a dilute granular flow can be written in the form

$$\partial_t f + \mathbf{v} \cdot \partial_{\mathbf{x}} f + \partial_{\mathbf{v}} \cdot \left(f \frac{\mathbf{F}}{m_{\mathrm{P}}} \right) = \mathbb{C}, \tag{2.1}$$

where $f(\mathbf{v}, \mathbf{x}, t)$ is the velocity-based density function, $\mathbf{v}$ is the particle velocity, $\mathbf{F}$ is the force acting on each particle, m_{p} is the particle mass, and $\mathbb{C}$ is the Boltzmann-Enskog collision term described in Appendix A, representing the rate of change in the velocity distribution function due to inelastic particle-particle collisions. Without loss of generality, hereinafter we will assume that f has been normalized so that its zero-order moment

is equal to the particle volume fraction α_s. In the case under examination, no external force is present in the system, so the term containing **F** can be dropped. To be consistent with the molecular dynamics (MD) simulations used for model validation, inelastic hard-sphere collisions between mono-disperse particles with diameter d_p and restitution coefficient e are considered. The local Knudsen number is defined by $\mathrm{Kn} = d_p/(6\alpha_s L)$, where L is the system size. In this work, the particle diameter is small relative to the system size ($d_p/L = 1/35$), but the solids volume fraction is small enough for Knudsen effects to be important. As described in Appendix A, the Boltzmann-Enskog collision term can be expanded in powers of d_p/L and the zero-order approximation is the Boltzmann collision integral, which does not account for finite-size particle effects present in the MD simulations. In particular, the collisional-flux contribution contained in the first-order terms of the Boltzmann-Enskog collision integral is neglected in the Boltzmann collision integral used in this work.

For inelastic hard-sphere collisions, the integral of the Boltzmann collision term used to compute the moments of f does not appear in closed form. In order to overcome this difficultly, a kinetic model can be used to approximate the Boltzmann collision integral in terms of a closed set of lower-order moments [13, 35]. In Appendix B, two types of kinetic models are introduced for inelastic hard-sphere collisions. The first is the inelastic Maxwell model [5, 10] wherein the collision cross-section is simplified to remove its explicit dependence on the instantaneous velocity difference g. This simplification, first proposed by [32] for elastic collisions, is particularly interesting for inelastic collisions because it retains the exact dependence on the restitution coefficient through the parameter $\omega = (1+e)/2$. In the second type of kinetic model, the collision term is approximated as a linear function of the velocity distribution (see Appendix B for details):

$$\mathbb{C} = \frac{1}{\tau}(f^* - f), \tag{2.2}$$

where $\tau = \zeta\sqrt{\pi}d_p/(12g_0\alpha_s\sqrt{T})$ is the characteristic collision time and f^* is an anisotropic Gaussian distribution defined by

$$f^* = \frac{\alpha_s}{\left[\det(2\pi\boldsymbol{\lambda})\right]^{1/2}}\exp\left[-\frac{1}{2}(v_i - U_{pi})(\boldsymbol{\lambda}^{-1})_{ij}(v_j - U_{pj})\right], \tag{2.3}$$

where repeated Roman indices imply summation. In this expression, $\mathbf{U}_p$ is the mean particle velocity and $\boldsymbol{\lambda}$ is a second-order tensor defined by

$$\boldsymbol{\lambda} = \zeta\omega^2 T\mathbf{I} + (\zeta\omega^2 - 2\zeta\omega + 1)\boldsymbol{\sigma}, \tag{2.4}$$

in which $\boldsymbol{\sigma}$ is the velocity covariance tensor, T is the granular temperature (equal to one third the trace of $\boldsymbol{\sigma}$), and ζ is a parameter whose value must be between 0 and 3/2 to ensure that $\boldsymbol{\lambda}$ is positive definite. It can be shown that, for $e = 1$, ζ is related to the Prandtl number Pr by $\zeta = 1/\mathrm{Pr}$ (see [35]), and thus ζ can be chosen to fix Pr. The radial distribution function on contact g_0, appearing in the collision time, is a function of α_s and accounts

for finite-size effects in the dense limit. Note that τ is proportional to Kn, and Knudsen effects occur when the collision time is the same order of magnitude as the time scale for the spatial transport term in the kinetic equation.

In the elastic limit ($\omega = 1$), setting $\zeta = 1$ [7,8] in Eq. (2.4) recovers the Bhatnagar-Gross-Krook (BGK) collision model [3]. The BGK collision model correctly degenerates to the Maxwellian limit at equilibrium, it satisfies the requirements of mass, momentum and energy conservation and the positivity criterion for the entropy production (H-theorem). However, the BGK model does not provide the correct value of Pr, which should be 2/3 for a mono-atomic gas [35]. The problem of achieving the correct Prandtl number was addressed by [28], who proposed the ellipsoidal statistical BGK (ES-BGK) model, given by Eqs. (2.2) and (2.4) with $\omega = 1$ and $\zeta = 3/2$. For simplicity, hereinafter we will continue to refer to *inelastic* cases with $\zeta = 1$ as the BGK model and with $\zeta = 3/2$ as the ES-BGK model. A similar collision model, with $\zeta \neq 1$, was proposed in [16].

In moment methods, the kinetic equation is not solved directly for the velocity distribution function, but the evolution in space and time of its moments is tracked through the solution of moment transport equations [35]. Using the same notation adopted in [19], the moments of the velocity distribution function $f(\mathbf{v};\mathbf{x},t)$ can be defined as

$$M_{ijk}^{\gamma}(\mathbf{x},t) = \int v_1^i v_2^j v_3^k f(\mathbf{v};\mathbf{x},t) \mathrm{d}\mathbf{v}, \tag{2.5}$$

where $\gamma = i+j+k$ is the order of the moment, and the non-negative integer values of i,j,k indicate the order of each velocity component. Starting from Eq. (2.1), moment transport equations are derived using the definition in Eq. (2.5). Neglecting the force term for the reason explained above, this leads to the transport equation for the γ-order moment:

$$\partial_t M_{ijk}^{\gamma} + \partial_{x_1} M_{i+1jk}^{\gamma+1} + \partial_{x_2} M_{ij+1k}^{\gamma+1} + \partial_{x_3} M_{ijk+1}^{\gamma+1} = C_{ijk}^{\gamma}, \tag{2.6}$$

where C_{ijk}^{γ} is the source term due to the moments of the collision operator. Eqs. (2.6) are not in closed form, because they contain the moment spatial fluxes, represented by the last three derivatives on the left-hand side of the equation. Moreover, the collision source term, in general, is not an explicit expression of the moments up to order γ. As will be discussed in detail later, the inelastic Maxwell, BGK, and ES-BGK collision models allow C_{ijk}^{γ} to be computed explicitly in terms of the moments, whereas this is not possible for the Boltzmann collision integral. As a consequence, for the Boltzmann collision integral it is necessary to derive consistent closures for C_{ijk}^{γ}, to be able to proceed in the solution of Eq. (2.6). This task is achieved in this work using Gaussian quadrature formulas, as explained in Section 3.

2.1 Boundary conditions

Moment methods require the wall distribution function to be specified in terms of the velocity distribution function next to the wall and the properties of particles after they

collide with the wall. Maxwell [32] proposed a generalized boundary condition for the velocity distribution function at the wall in the form [35]

$$f_{\rm w} = \begin{cases} \chi f_{\rm eq,w} + (1-\chi)f_{\rm r,w}\left(-|\mathbf{v}-\mathbf{U}_{\rm p}|_{\perp,{\rm w}}\right), & \text{if } |\mathbf{v}-\mathbf{U}_{\rm p}|_{\perp{\rm w}} > 0, \\ f_{\rm r,w}\left(|\mathbf{v}-\mathbf{U}_{\rm p}|_{\perp,{\rm w}}\right), & \text{if } |\mathbf{v}-\mathbf{U}_{\rm p}|_{\perp,{\rm w}} \leqslant 0, \end{cases} \tag{2.7}$$

where $|\mathbf{v}-\mathbf{U}_{\rm p}|_{\perp,{\rm w}}$ represents the magnitude of the particle peculiar velocity normal to the wall, and χ is the accommodation coefficient. For $\chi=0$, the boundary condition returns the specular reflective wall condition with distribution $f_{\rm r,w}$, which corresponds to a change in sign of the particle velocity normal to the wall, while for $\chi=1$, the distribution $f_{\rm eq,w}$ corresponds to the Maxwellian at the wall temperature $T_{\rm w}$, which defines the diffuse reflective with full accommodation boundary condition. In this work we assume $\chi=1$ to be consistent with the MD simulations. Note that by using the definition of the moments in Eq. (2.5), it is straightforward to compute the moments at the walls given $f_{\rm w}$.

It is worth noting that in hydrodynamic models for granular flow, based on an expansion valid for small Knudsen numbers [14], the boundary conditions are expressed in terms of the gradients of the hydrodynamic variables. However, it is difficult to derive boundary conditions that yield the correct behavior for all types of particle-wall interactions (e.g., specular reflections) for these models. In particular, the boundary conditions break down for granular flows with Knudsen layers and must be modified to account for phenomena like slip and temperature jump at walls. In contrast, in moment methods, since the boundary conditions for the moments are found from the velocity distribution function at the wall $f_{\rm w}$, they are, in principle, valid for arbitrary Knudsen numbers and any type of particle-wall interaction.

3 Quadrature-based moment method

In quadrature-based moment methods [18, 19], Gaussian quadrature formulas are used to provide closures for the spatial fluxes and source terms in the moment transport equations, by introducing a set of weights ρ_α, which are positive as a consequence of properties of the Gaussian quadrature formulas, and a set of abscissas $\mathbf{U}_\alpha = (u_{1\alpha}, u_{2\alpha}, u_{3\alpha})$. The weights and abscissas are determined from the moments of the distribution function using an inversion algorithm, which was developed in [18,19], and is briefly outlined in this section. Once the weights and abscissas are computed, the velocity distribution function can be represented by a sum of Dirac delta functions:

$$f(\mathbf{v}) = \sum_{\alpha=1}^{N} \rho_\alpha \delta(\mathbf{v}-\mathbf{U}_\alpha). \tag{3.1}$$

Through the moment-inversion algorithm, this distribution function is uniquely determined for a given set of velocity moments, and, as shown below, it can be used to close the moment transport equations.

The definition of the moment-inversion algorithm is done in terms of the rotated central moments R_{ijk}^{γ}, obtained from the moments in M_{ijk}^{γ} by applying a linear transformation $\mathbf{L}$, so that the moments are translated with respect to the mean velocity and rotated so that the velocity covariance matrix becomes diagonal. This operation is required to ensure that the inversion algorithm produces positive weights when the velocity covariances are far from zero [19], which is likely to happen under conditions far from the equilibrium. In the following discussion, the set of $N = n^3$ abscissas in the rotated central frame are

$$\mathbf{R}_\alpha = (r_{1\alpha}, r_{2\alpha}, r_{3\alpha}),$$

where n is the number of quadrature nodes used in each spatial direction. It is worth noting that the quadrature weights ρ_α are not affected by the transformation, while the velocity abscissas in the original frame $\mathbf{U}_\alpha$ can be recovered from

$$\mathbf{U}_\alpha = \mathbf{L}^{\mathrm{T}}\mathbf{R}_\alpha + \mathbf{U}_{\mathrm{p}}. \tag{3.2}$$

Also, due to the lack of mean velocity gradients in the system under consideration in this work, the velocity covariance matrix will be diagonal. Thus, the matrix $\mathbf{L}$ will be diagonal for all the cases considered in Section 6.

The multi-dimensional quadrature formula is defined by considering a set of $2n$ moments in each direction (e.g., $R_{000}^0, \cdots, R_{002n-1}^{2n-1}$), which are used to compute a set of n univariate weights and abscissas in each spatial direction, using one of the flavors the product-difference (PD) algorithm [27, 33, 37]. The velocity abscissas $\mathbf{R}_\alpha$ are then defined through the tensor product of the univariate abscissas in each direction. The last operation consists in finding the weights ρ_α, which are computed by solving a system of n^3 linear equations. The first $3n-2$ linear equations are obtained by imposing that the weights of the multidimensional quadrature formula satisfy the univariate weight constraints, while the remaining $n^3 - 3n + 2$ equations come from fixing the set of mixed moments with indices up to $n-1$ (e.g., $R_{110}^2, \cdots, R_{n-1n-1n-1}^{3n-3}$) and by expressing them in terms of the quadrature weights and abscissas [19]. Once weights and abscissas are known, Eq. (3.2) is applied to find the abscissas in the original frame, and then the velocity moments can be evaluated as

$$M_{ijk}^{\gamma} = \sum_{\alpha=1}^{N} \rho_\alpha u_{1\alpha}^i u_{2\alpha}^j u_{3\alpha}^k. \tag{3.3}$$

As discussed below, any other unclosed term in the moment equations (e.g., the Boltzmann collision integral) can be expressed in terms of the weights and abscissas. By virtue the properties of the algorithm, Eq. (3.3) is an identity for the n^3 moments used in the moment-inversion algorithm. For the remaining moments, Eq. (3.3) provides an optimal approximation in the sense of Gaussian quadrature [27, 33, 37].

3.1 Closure of moment spatial fluxes

The moment spatial fluxes are closed according to their kinetic description [15, 18, 34]. First, the moments involved in the spatial fluxes are decomposed in two contributions:

$$M_{i+1jk}^{\gamma+1} = Q_{1,ijk}^{-} + Q_{1,ijk}^{+}, \tag{3.4a}$$

$$M_{ij+1k}^{\gamma+1} = Q_{2,ijk}^{-} + Q_{2,ijk}^{+}, \tag{3.4b}$$

$$M_{ijk+1}^{\gamma+1} = Q_{3,ijk}^{-} + Q_{3,ijk}^{+}, \tag{3.4c}$$

with

$$Q_{n,ijk}^{-} = \int \min(\mathbf{e}_n \cdot \mathbf{v}, 0) v_1^i v_2^j v_3^k f(\mathbf{v}) d\mathbf{v}, \tag{3.5a}$$

$$Q_{n,ijk}^{+} = \int \max(\mathbf{e}_n \cdot \mathbf{v}, 0) v_1^i v_2^j v_3^k f(\mathbf{v}) d\mathbf{v}, \tag{3.5b}$$

where $\mathbf{e}_n$ is the Cartesian unit vector in direction n. The integrals in the definition of the two components $Q_{n,ijk}^{-}$ and $Q_{n,ijk}^{+}$ are then approximated by replacing the integrals in (3.5) with the corresponding quadrature approximation using (3.1):

$$Q_{n,ijk}^{-} = \sum_{\alpha=1}^{N} \rho_\alpha \min(\mathbf{e}_n \cdot \mathbf{u}_\alpha, 0) u_{1\alpha}^i u_{2\alpha}^j u_{3\alpha}^k, \tag{3.6a}$$

$$Q_{n,ijk}^{+} = \sum_{\alpha=1}^{N} \rho_\alpha \max(\mathbf{e}_n \cdot \mathbf{u}_\alpha, 0) u_{1\alpha}^i u_{2\alpha}^j u_{3\alpha}^k. \tag{3.6b}$$

The reader should note that the decomposition of the moment involved in the evaluation of the spatial fluxes in two components is only necessary for the numerical solution of the moment transport equations. By definition, kinetic-based fluxes combined with a finite-volume method ensure the realizability of the transported moments and exactly reproduce particle trajectory crossing [15]. This would not be generally true if traditional interpolation methods were used to compute the moment spatial fluxes. It is worth noting that the realizability condition of the transported moments is guaranteed if a first-order interpolation scheme is employed to evaluate the cell-face values of weights and abscissas used in the computation of the fluxes [15]. However particular care has to be taken when adopting high-order interpolation schemes, since the condition of moment realizability is not automatically satisfied. High-order realizable interpolation schemes for quadrature-based moment methods are developed in [36].

3.2 Closure of the collision term

The BGK and ES-BGK collision models allow explicit expressions for the rates of change of the moments due to collisions to be found by applying the moments definition (2.5) to Eq. (2.2):

$$C_{ijk}^{\gamma} = \frac{1}{\tau} (\Delta_{ijk}^{\gamma} - M_{ijk}^{\gamma}), \tag{3.7}$$

where Δ_{ijk}^{γ} is the set of moments of order γ of the equilibrium distribution function, which is obtained by replacing f with f^* in Eq. (2.5). Explicit closures cannot be obtained for the Boltzmann collision integral. However, it is possible to approximate the collision integral using the weights and abscissas of the quadrature approximation. The procedure to derive the closure with hard-sphere collisions is fairly complicated, and is explained in [22]. Only the resulting moment source terms are reported here.

The moments of the hard-sphere Boltzmann collision integral can be written in the form

$$C_{ijk}^{\gamma} = \frac{6g_0}{d_p} \int_{\mathbb{R}^3} \int_{\mathbb{R}^3} g I_{ijk}(\omega, \mathbf{v}_1, \mathbf{g}) f(\mathbf{v}_1) f(\mathbf{v}_2) d\mathbf{v}_1 d\mathbf{v}_2, \tag{3.8}$$

where

$$I_{ijk} = \frac{1}{\pi g} \int_{S^+} \left[(v_{1,1}')^i (v_{1,2}')^j (v_{1,3}')^k - (v_{1,1})^i (v_{1,2})^j (v_{1,3})^k \right] |\mathbf{g} \cdot \mathbf{n}| d\mathbf{n}, \tag{3.9}$$

$\mathbf{g} = \mathbf{v}_1 - \mathbf{v}_2$ the relative velocity vector with magnitude g, $\mathbf{n}$ the unit vector along the line containing the two colliding particles centers, $\mathbf{v}_1' = \mathbf{v}_1 - \omega(\mathbf{g} \cdot \mathbf{n})\mathbf{n}$, and $\omega = (1+e)/2$. The inelastic Maxwell model (see Appendix B) has the same form as Eq. (3.8), but with g replaced by the average value $\langle g \rangle$.

The integral over the collision cross-section S^+ in Eq. (3.9) can be evaluated explicitly for non-negative values of i, j and k by writing it in terms of multinomial expansions. To achieve this result, an orthonormal transformation $\mathbf{L}_c(\mathbf{g})$ is applied to transform the laboratory frame of reference $\mathbf{x}$ into the collision frame of reference $\mathbf{x}^\dagger$, so that $\mathbf{x}^\dagger = \mathbf{L}_c \mathbf{x}$. Conventionally we assume the relative velocity vector $\mathbf{g}$ to be aligned with the $x_3^\dagger$ direction, leading to the following transformation matrix:

$$\mathbf{L}_c = \begin{bmatrix} \sin\phi_1 & -\cos\phi_1 & 0 \\ \cos\theta_1\cos\phi_1 & \cos\theta_1\sin\phi_1 & -\sin\theta_1 \\ \sin\theta_1\cos\phi_1 & \sin\theta_1\sin\phi_1 & \cos\theta_1 \end{bmatrix}, \tag{3.10}$$

where $0 \leqslant \theta_1 \leqslant \pi$, and $0 \leqslant \phi_1 \leqslant 2\pi$ are spherical angles related to $\mathbf{g}$ by $g_1 = g\sin\theta_1\cos\phi_1$, $g_2 = g\sin\theta_1\sin\phi_1$, and $g_3 = g\cos\theta_1$. By means of this transformation, the integral in Eq. (3.9) is rewritten as an integral over the collision angles θ and ϕ:

$$I_{ijk} = \frac{1}{\pi} \int_0^{2\pi} \int_0^{\frac{\pi}{2}} \left[(v_{1,1}')^i (v_{1,2}')^j (v_{1,3}')^k - (v_{1,1})^i (v_{1,2})^j (v_{1,3})^k \right] \cos\theta\sin\theta d\theta d\phi, \tag{3.11}$$

where

$$\mathbf{v}_1' = \mathbf{v}_1 - (\omega g\cos\theta)\mathbf{L}_c^{\mathsf{T}}\mathbf{n}^\dagger, \quad \text{and} \quad \mathbf{n}^\dagger = (\sin\theta\cos\phi, \sin\theta\sin\phi, \cos\theta).$$

Rewriting the powers of the post-collisional velocity components (e.g., $(v_{1,1}')^i$) as multinomial expansions, functions of the pre-collisional velocities, the relative velocity and the collision angles, and explicitly integrating over the collision angles, Eq. (3.11) becomes

$$I_{ijk} = \sum_{i_1=0}^{i} \sum_{i_2=0}^{j} \sum_{i_3=0}^{k} (-\omega g)^{i_1+i_2+i_3} S_{i_1 i_2 i_3}(\theta_1, \phi_1) \binom{i}{i_1} \binom{j}{i_2} \binom{k}{i_3} v_{1,1}^{i-i_1} v_{1,2}^{j-i_2} v_{1,3}^{k-i_3}, \tag{3.12}$$

where $S_{000} = 0$, and for $i_1 + i_2 + i_3 > 0$,

$$S_{i_1 i_2 i_3} = \sum_{j_1=0}^{i_1} \sum_{j_2=0}^{i_2} \sum_{j_3=0}^{i_3} \sum_{k_1=0}^{j_1} \sum_{k_2=0}^{j_2} \sum_{k_3=0}^{j_3} \binom{i_1}{j_1} \binom{i_2}{j_2} \binom{i_3}{j_3} \binom{j_1}{k_1} \binom{j_2}{k_2} \binom{j_3}{k_3}$$
$$L_{c,11}^{i_1-j_1} L_{c,12}^{i_2-j_2} L_{c,13}^{i_3-j_3} L_{c,21}^{j_1-k_1} L_{c,22}^{j_2-k_2} L_{c,23}^{j_3-k_3} L_{c,31}^{k_1} L_{c,32}^{k_2} L_{c,33}^{k_3} K_{ijk}, \tag{3.13}$$

with $i = i_1 + i_2 + i_3$, $j = j_1 + j_2 + j_3$ and $k = k_1 + k_2 + k_3$. The constants K_{ijk} resulting from integration over the collision angles are defined as

$$K_{ijk} = A_{i-1,j-k} B_{i+k,i-k},$$

where

$$A_{a,b} \equiv \frac{1}{\pi} \int_0^{2\pi} (\cos\phi)^a (\sin\phi)^b \mathrm{d}\phi = [1+(-1)^a] [1+(-1)^b] \frac{1}{2\pi} B\left(\frac{a+1}{2}, \frac{b+1}{2}\right), \tag{3.14a}$$

$$B_{c,d} \equiv \int_0^{\frac{\pi}{2}} (\cos\theta)^{c+1} (\sin\theta)^{d+1} \mathrm{d}\theta = \frac{1}{2} B\left(\frac{c+2}{2}, \frac{d+2}{2}\right). \tag{3.14b}$$

$B(x,y)$ is the beta function, defined in terms of Euler gamma function as

$$B(x,y) = \frac{\Gamma(x)\Gamma(y)}{\Gamma(x+y)}.$$

At this point, I_{ijk} can be computed for any given values of ω, $\mathbf{v}_1$, and $\mathbf{g}$. We can now apply the quadrature formula (3.1) to evaluate the two integrals over the velocity distribution function in (3.8). Doing so, the collision source term for the moment equations becomes

$$C_{ijk}^{\gamma} = \frac{6g_0}{d_{\mathrm{P}}} \sum_{\alpha=1}^{N} \sum_{\beta=1}^{N} \rho_\alpha \rho_\beta g_{\alpha\beta} I_{ijk}(\omega, \mathbf{u}_\alpha, \mathbf{g}_{\alpha\beta}), \tag{3.15}$$

where $\mathbf{g}_{\alpha\beta} = \mathbf{u}_\alpha - \mathbf{u}_\beta$, and $g_{\alpha\beta} = |\mathbf{g}_{\alpha\beta}|$. Using (3.15), the inelastic hard-sphere Boltzmann collision integral can be approximated in the moment transport equations once the quadrature weight and abscissas are known. Note that, because the integrals over the collision angles were carried out explicitly, the approximation in (3.15) inherits all of the conservation properties of the Boltzmann collision integral. For a homogeneous system, the long-time solution found using (3.15) has isotropic central moments. However, as discussed in Appendix C, the non-zero central moments of orders higher than two are Gaussian only in the "$\lim_{N\to\infty}$" due to the discrete representation of the distribution function. The inelastic Maxwell model is computed from Eq. (3.15) by replacing $g_{\alpha\beta}$ with $\langle g \rangle$, where

$$\langle g \rangle = \frac{1}{\alpha_{\mathrm{s}}^2} \sum_{\alpha=1}^{N} \sum_{\beta=1}^{N} \rho_\alpha \rho_\beta g_{\alpha\beta} \tag{3.16}$$

is computed using quadrature. For homogeneous elastic systems, the central moments found from the inelastic Maxwell model are Gaussian. We should note that, relative to the BGK model, calculation of C_{ijk}^{γ} via (3.15) is computationally expensive due to the double summation over N and the complexity of I_{ijk} for higher-order moments.

3.3 Quadrature-based boundary conditions for the moments

The implementation of the diffuse reflective with full accommodation boundary condition in the quadrature-based moment method is obtained by initially considering the set of isotropic Gaussian moments with unit variance at the wall up to the order of moments considered. From this set of moments, a corresponding temporary set of weights $\rho_{w\alpha}$ and abscissas $\mathbf{U}_{w\alpha}$ at the wall are found by applying the moment-inversion algorithm. This set of abscissas is then rescaled to obtain the correct wall temperature:

$$\mathbf{U}_{w\alpha} \rightarrow \mathbf{U}_{w\alpha} \sqrt{T_w}. \tag{3.17}$$

In the case of moving walls, the wall tangential velocity would be added to the abscissas in the corresponding direction. However, in this work only stationary walls are considered, and this step is unnecessary.

At this point, the incoming and outgoing fluxes normal to the wall are computed in terms of the weights and abscissas. The formulation for plane walls is presented here. Let $\mathbf{w}$ be the unit wall-normal vector pointing into the fluid. The incoming flux from the fluid to the wall is given by

$$G_{w,in} = -\sum_{\alpha=1}^{N} \min(0, \mathbf{w} \cdot \mathbf{U}_{\alpha}^{*}) \rho_{\alpha}^{*}, \tag{3.18}$$

while the outgoing flux from the wall to the fluid is

$$G_{w,out} = \sum_{\alpha=1}^{N} \max(0, \mathbf{w} \cdot \mathbf{U}_{w\alpha}) \rho_{w\alpha}, \tag{3.19}$$

where $\mathbf{U}_{\alpha}^{*}$ is the velocity abscissa in the fluid adjacent the wall and ρ_{α}^{*} is the corresponding quadrature weight. Once the fluxes $G_{w,in}$ and $G_{w,out}$ are known, the temporary quadrature weights at the wall are rescaled to satisfy the continuity constraint:

$$\rho_{w\alpha} \rightarrow \rho_{w\alpha} \frac{G_{w,in}}{G_{w,out}}, \tag{3.20}$$

and the moments are recomputed from (3.3) using the updated set of weights and abscissas. Note that this procedure is equivalent to representing the equilibrium wall distribution function by

$$f_{eq,w}(\mathbf{v}) = \sum_{\alpha=1}^{N} \rho_{w\alpha} \delta(\mathbf{v} - \mathbf{U}_{w\alpha}). \tag{3.21}$$

By construction, $f_{eq,w}$ is Maxwellian and conserves the normal mass flux at the wall.

The implementation of the diffuse reflective condition explained above must be modified slightly when the full Boltzmann collision model is used. As mentioned earlier, the quadrature closure of the Boltzmann collision integral does not generate Gaussian moments (maximum relative difference equal to 3.2% for $N = 64$ and $e = 1$, see Appendix C).

As a consequence, to be consistent with the quadrature closure used in the interior of the domain, a homogeneous case with elastic mono-dispersed particles interacting due to collisions was used to compute the velocity moments at the wall. The moments provided by the quadrature closure of the Boltzmann collision integral were computed when the system reached a self-similar state, and this set of moments was used to replace the set of Maxwellian moments at the wall when the Boltzmann collision model was adopted. Note that this modification will ensure that when $e=1$ and the walls all have the same temperature (i.e., an isothermal, elastic system), the velocity distribution function in the fluid will be the same as the for the walls.

Because the quadrature-based moment method results in an explicit representation of wall distribution function f_w in terms of the weights and abscissas, it is straightforward to derive the moment boundary conditions for moments of arbitrary order. The general procedure for an arbitrary wall distribution function is as follows: (i) compute all of the central moments needed for the moment-inversion algorithm from f_w, (ii) apply the moment-inversion algorithm to find $\rho_{w\alpha}$ and $\mathbf{U}_{w\alpha}$, (iii) use these weights and abscissas to approximate the distribution function at the wall that appears in the expression of the boundary condition (Eq. (2.7)). This allows any form of boundary condition written in terms of the velocity distribution function to be implemented in the quadrature-based moment method. Note that phenomena such as partial slip at the walls for the mean velocity and temperature are not imposed, but rather are a result of the model. The definition of the moment-inversion algorithm, of the source term closures for the moment transport equations and of the boundary conditions provided in this section lead to a closed set of partial differential equations, which can be solved numerically.

4 Solution algorithm for the moment transport equations

The moment transport equations can be solved using the finite-volume method [15, 17]. For sake of simplicity, we denote the set of moments M_{ijk}^{γ} by $\mathbf{M}$, the set of weights and abscissas by $\mathbf{N}=[\rho_{\alpha},\mathbf{U}_{\alpha}]$, the spatial fluxes computed as a function of the weights and abscissas by $\mathbf{Q}^-$ and $\mathbf{Q}^+$, and the collision terms by $\mathbf{C}$. With this new notation, Eq. (2.6) can be rewritten as

$$\partial_t\mathbf{M}+\partial_{\mathbf{x}}\cdot(\mathbf{Q}^-+\mathbf{Q}^+)=\mathbf{C}. \tag{4.1}$$

Due to the nature of the collision term, this equation can be solved by using a time-splitting scheme wherein the spatial fluxes and collisions are treated sequentially.

The spatial fluxes need to be treated with special care, to ensure the realizability of the set of moments. If we denote the flux function by

$$\mathbf{G}(\mathbf{N}^-,\mathbf{N}^+)=\mathbf{Q}^-+\mathbf{Q}^+,$$

the updated moments $\mathbf{M}^*$ can be computed from

$$\mathbf{M}^*=\mathbf{M}-\frac{\Delta t}{\Delta \mathbf{x}}\cdot\left[\mathbf{G}(\mathbf{N}_r^-,\mathbf{N}_r^+)-\mathbf{G}(\mathbf{N}_l^-,\mathbf{N}_l^+)\right],$$

where the subscripts *l* and *r* refer to the direction considered when performing the interpolation of the weights and abscissas at the left and right cell faces, respectively. Because a first-order interpolation scheme is known to guarantee realizable moments [15], this scheme is used in this work to approximate the values of weights and abscissas on cell faces.

The change in the set of moments due to collisions is then computed by evaluating the local collision time as a function of **M** and explicitly integrating the collision term over time, solving

$$\frac{d\mathbf{M}^*}{dt} = \mathbf{C}.$$

Integration in time is performed using a two-step explicit Runge-Kutta method, determining the time step on the basis of the collision time τ and of the Courant number based on the maximum velocity abscissa [15][‡]. In the collision models, the radial distribution function is approximated by a slight variation of the model for rigid spheres [9]:

$$g_0 = \frac{2-c}{2(1-c)^3} + 1.1603c, \tag{4.2}$$

where $c = \alpha_s / \alpha_{\max}$, and $\alpha_{\max} = 0.63$ is the maximum packing limit for the solids volume fraction. In this work we are interested in dilute flows with $\alpha_s \leq 0.05$, and the second term on the right-hand side of (4.2) was fitted to the MD data of [1] for g_0 at $\alpha_s = 0.0501$.

5   Description of the system and simulation conditions

The system under examination in this work, investigated previously using MD simulations [23], is constituted by a quiescent granular flow made of spherical, frictionless and inelastic particles between two stationary walls of constant set temperatures T_C and T_H, with $T_C \leqslant T_H$, as schematically represented in Fig. 1. The remaining four walls are periodic. Particles are not influenced by any external force, as a consequence the system is characterized by the absence of mean motion. In the QMOM results the walls are described as diffuse reflective with full accommodation boundary conditions [12], meaning that particles are reflected by the walls with a velocity sampled from a Maxwellian distribution, consistent with the set wall temperature. At the beginning of each simulation, α_s is distributed uniformly in the system with an average volume fraction $\overline{\alpha}$ depending

---

[‡]The simulations performed in this work admit a steady state. As a consequence, a steady-state solver could be used instead of integrating in time. This would significantly reduce the computational cost. This was not done in the present work, since the computational cost of the unsteady simulation is low as discussed elsewhere in this manuscript, and the code where QMOM was implemented is unsteady. As an indication, the computational time required to perform one unsteady simulation with 64-node QMOM, using a Matlab code, on a quad-core Intel Xeon processor at 3 GHz, with real time plotting of the results at each time step, is of about 30 minutes to achieve the full steady state, with BGK-like models. Each case of MD simulations required an average of 2 days of computational time on a single Pentium IV at 2.53 GHz processor with a C code compiled with the GNU C compiler (gcc).
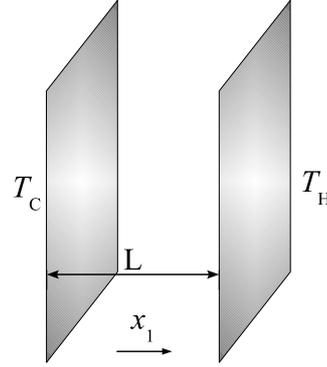
Figure 1: Schematic representation of the bounded conduction system.

on the case considered (see Table 1). A linear temperature profile is used as initial condition for the simulations, whose slope depends on the temperature of the two walls. A Maxwellian distribution is adopted for the initial velocity distribution function. Results provided by QMOM are reported once the numerical solution reached steady state and compared to the MD simulations described elsewhere [23].

Table 1: Simulation test cases and corresponding conditions and particle properties.

Case	T_C	T_H	$\overline{\alpha}$	e	Kn
1	0.5	1	0.05	1	0.095
2	0.5	1	0.05	0.99	0.095
3	2/3	2/3	0.025	0.99	0.191
4	2/3	2/3	0.025	0.96	0.191
5	2/3	2/3	0.025	0.9	0.191

The significant parameters of the simulation are the wall temperatures T_C and T_H, the average particle volume fraction $\overline{\alpha}$, and the restitution coefficient e for collisions between particles. The characteristic length of the system is $L = 1$, and $L/d_p = 35$ in all the MD simulations [23]. Different conditions were examined as reported in Table 1, where the average Knudsen number is defined as $Kn = d_p/(6\overline{\alpha}L)$. One-dimensional QMOM calculations were performed with the four different collision models described in Section 2. A finite-volume method with a uniform spatial discretization of 120 grid cells in the direction orthogonal to the walls was employed. As described in Appendix A, the zero-order approximation to the Boltzmann-Enskog collision integral does not include finite-size-particle effects and thus, strictly speaking, is comparable to MD simulations with $L/d_p \gg 1$. In order to judge the magnitude of the finite-particle effects in the MD simulations with $L/d_p = 35$, for some of the statistics we will present MD results for the kinetic and collisional-flux parts separately. The latter are computed as described in [23]. For the QMOM calculations, only the kinetic parts of the velocity statistics are included in the collision models.

In the QMOM calculations, the solids volume fraction is found directly from the zero-order moment. All other statistics are reported in dimensionless form using a characteristic granular temperature equal to one. The mean particle velocities are defined by $\mathbf{U}_p = (M^1_{100}, M^1_{010}, M^1_{001})/\alpha_s$. The mean velocities parallel to the walls are null for all times, while the wall-normal component of the mean velocity (U_{p1}) becomes null only at steady state. The granular temperature components and the granular temperature are computed as

$$T_1 = \frac{M^2_{200}}{\alpha_s} - \left(\frac{M^1_{100}}{\alpha_s}\right)^2, \qquad T_2 = \frac{M^2_{020}}{\alpha_s} - \left(\frac{M^2_{010}}{\alpha_s}\right)^2, \tag{5.1a}$$

$$T_3 = \frac{M^2_{002}}{\alpha_s} - \left(\frac{M^3_{001}}{\alpha_s}\right)^2, \qquad T = \frac{1}{3}(T_1 + T_2 + T_3). \tag{5.1b}$$

By symmetry, the components parallel to the walls are equal ($T_2 = T_3$). The kinetic contribution to the diagonal stress tensor components are then evaluated by multiplying the temperature components by the solids volume fraction:

$$\sigma_{11} = \alpha_s T_1, \qquad \sigma_{22} = \alpha_s T_2, \qquad \sigma_{33} = \alpha_s T_3, \tag{5.2}$$

while the off-diagonal components are obtained as

$$\sigma_{12} = \alpha_s \left(\frac{M^2_{110}}{\alpha_s} - \frac{M^1_{100}}{\alpha_s}\frac{M^1_{010}}{\alpha_s}\right), \tag{5.3a}$$

$$\sigma_{13} = \alpha_s \left(\frac{M^2_{101}}{\alpha_s} - \frac{M^1_{100}}{\alpha_s}\frac{M^1_{001}}{\alpha_s}\right), \tag{5.3b}$$

$$\sigma_{23} = \alpha_s \left(\frac{M^2_{011}}{\alpha_s} - \frac{M^1_{010}}{\alpha_s}\frac{M^1_{001}}{\alpha_s}\right). \tag{5.3c}$$

By symmetry, the components parallel to the walls are equal ($\sigma_{22} = \sigma_{33}$). For the system under consideration the off-diagonal components should be null for all times, and this is confirmed by the simulations. For finite-size particles (e.g., the MD simulations), the stress tensor contains an additional term due to the collisional fluxes [22, 23], not present in the QMOM calculations, which scales like $T\alpha_s^2$. Thus, we can anticipate that Eq. (5.2) will slightly underestimate the MD results for the values of α_s considered here. As noted above, the MD results for the kinetic and collisional-flux parts of the stress tensor will be plotted separately for comparison with the QMOM results.

The heat flux in the wall-normal direction is calculated as

$$q_1 = \frac{1}{2}(M^3_{300} + M^3_{120} + M^3_{102}) + \frac{1}{2}\alpha_s U^3_{p1} - U_{p1}(M^2_{200} + \alpha_s T). \tag{5.4}$$

At steady state, $U_{p1} = 0$ within the numerical accuracy of the finite-volume scheme. The heat fluxes in the directions parallel to the walls should be null for all times, and this is confirmed by the simulations. As with the stress tensor, the heat flux in the MD data

contains an additional contribution due to the collisional fluxes [22, 23], not present in the QMOM calculations. We can again anticipate that (5.4) will underestimate the MD results.

Depending on the order of the quadrature, the moment method used in this work computes moments of order higher than three, which have not been reported for the MD simulations. In all cases, the moment method computes the moments up to second order. For the 8-node quadrature, only four of the ten third-order moments are computed and the remaining six are approximated using quadrature. For 27-node quadrature, all of the moments up to third order are computed, along with some moments up to sixth order. For 64-node quadrature all moments up to fourth order are computed, along with some moments up to ninth order. In order to quantify the degree of non-Gaussian behavior, we define the standardized central moments as

$$Q_{ijk}^{\gamma} = \left(\alpha_s T_1^{\frac{i}{2}} T_2^{\frac{j}{2}} T_3^{\frac{k}{2}}\right)^{-1} \int (v_1 - U_{\mathrm{p}1})^i (v_2 - U_{\mathrm{p}2})^j (v_3 - U_{\mathrm{p}3})^k f(\mathbf{v}) \mathrm{d}\mathbf{v}, \qquad (5.5)$$

which at steady state reduces to $Q_{ijk}^{\gamma} = M_{ijk}^{\gamma} \left(\alpha_s T_1^{i/2} T_2^{j/2} T_3^{k/2}\right)^{-1}$. Some of the non-zero, steady-state, standardized moments found from the QMOM calculations will be compared to the Gaussian values for selected cases.

6 Results and discussion

Results obtained from the QMOM calculations in the five different cases under examination are reported in this section and compared to results from the MD simulations.

6.1 Effect of the number of quadrature nodes

The accuracy of the quadrature-based moment method as a function of the number of quadrature nodes was studied using the BGK model for Cases 1 and 2 of Table 1. The solids volume fraction, granular temperature, and heat-flux profiles are reported in Fig. 2. Note that the *temperature slip* at the walls (i.e., the difference between the wall and fluid temperatures) is not an input to the moment method, but rather a prediction that follows from the prescribed boundary conditions. For all cases investigated, the temperature slip is well predicted by QMOM. However, due to finite-size effects in the MD simulations, one should expect some differences near the walls (i.e., the impinging particles change temperature at a finite distance $d_{\mathrm{p}}/2$ from the walls due to the size-exclusion effect [23]).

With elastic collisions (Case 1), the QMOM calculations provide satisfactory results for the solids volume fraction profile in all the cases considered with 8, 27 and 64 quadrature nodes with a slight improvement in the predictions with a higher number of nodes (Fig. 2(a)). A similar trend is observed in the predictions of the temperature profiles for the same conditions (see Fig. 2(c)). However, the introduction of a slight degree of in-elasticity (Case 2) shows that the 8-node quadrature closure leads to erroneous predictions in the shape of the solids volume fraction profile (Fig. 2(b)), with a peak in the
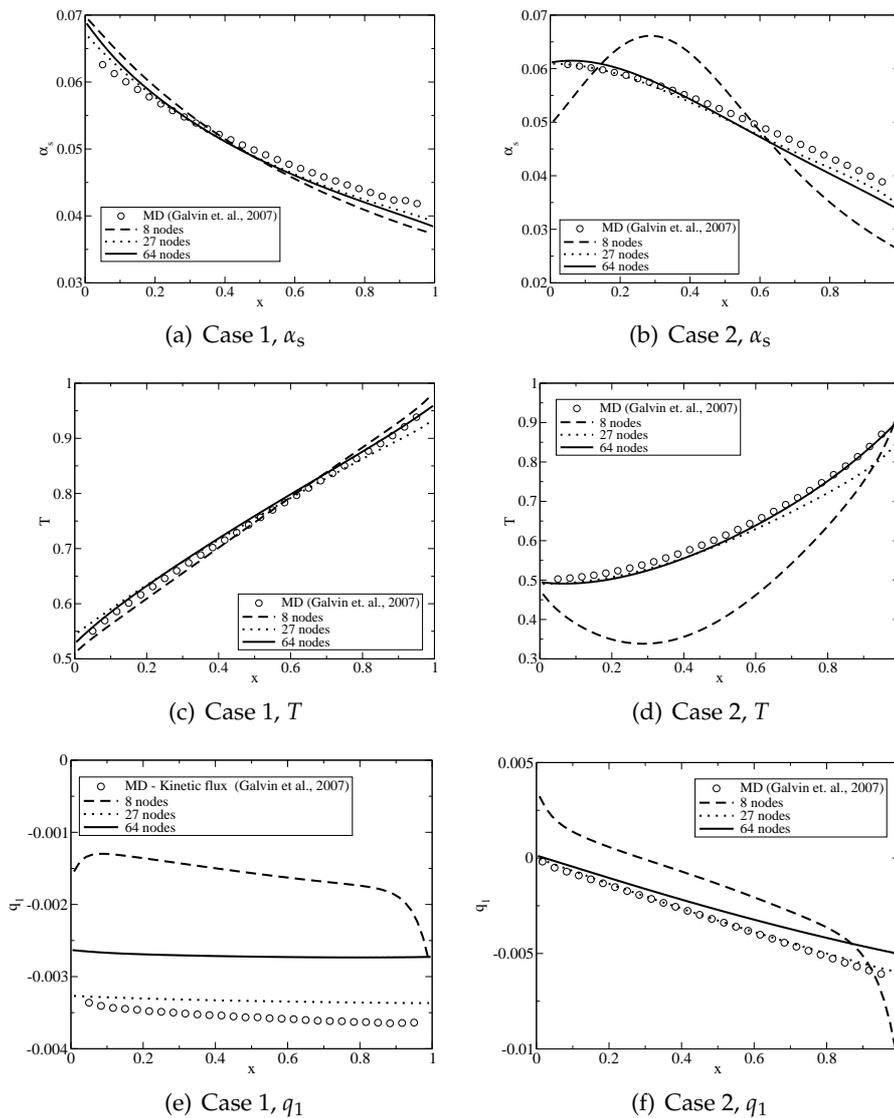
Figure 2: Profiles for solids volume fraction, granular temperature, and heat flux in Cases 1 and 2 for QMOM calculations with the BGK collision model using 8, 27, and 64 quadrature nodes.

particle concentration away from the cold wall, and to the under-estimation of the temperature (Fig. 2(d)), which indicates that either the energy dissipation is overpredicted or the heat flux from the walls in underpredicted. The accuracy in the solids volume fraction and temperature profiles observed in the case of elastic collisions is recovered with a higher number of nodes, with very satisfactory agreement between MD and QMOM calculations results with 64 nodes.

Insight into the reasons for the discrepancy observed with the 8-node quadrature can be obtained by examining the heat flux, whose profiles are reported in Fig. 2. Most re-

markably, despite the lack of the collisional-flux term due to finite-size effects, the 27-and 64-node quadratures yield good predictions for the heat flux for Case 2. The heat flux depends on the third-order moments of the velocity distribution function, which are not completely controlled by the 8-node quadrature approximation due to the constraints imposed by the quadrature formula[§]. Moreover the third-order moment transport equations depend on the fourth-order moment spatial fluxes, which are only approximated by the 8-node quadrature [19]. This source of approximation is not present with the higher-order quadratures considered in this work, because 27-node quadrature allows moments up to the fifth order to be controlled, and 64-node quadrature increases the order of controlled moments to seven, allowing all the third- and fourth-order moments to be controlled. Consequently only the 64-node quadrature is considered in the remainder of this work. However, we should note that 27-node quadrature provides reasonably accurate predictions at relatively lower cost than 64-node quadrature, and that the poor predictions of the heat flux with 8-node quadrature are consistent with previous observations [19].

6.2   Comparison of the four collision models

In this section the predictions obtained with the four collisions models (BGK, ES-BGK, inelastic Maxwell, full Boltzmann) in the QMOM calculations are compared to establish their accuracy with respect to the MD results. Cases 1 and 2 have an imposed mean temperature gradient. As shown in Fig. 3, very similar predictions for the solids volume fraction and temperature are obtained with all four collision models in Case 1, and all collision models are in good agreement with the MD simulations. Results for Case 2, where the collisions between particles are slightly inelastic, show that the ES-BGK model provides results for the particle temperature profile in slightly better agreement with the MD data than the other collision models (Fig. 3(d)). However, the inelastic Maxwell model leads to very good predictions. We can conclude that all four collision models perform adequately for Case 2, although the full Boltzmann model tends to underpredict the temperature. Overall, for both cases with imposed mean temperature gradients the QMOM calculations exhibit good agreement with the MD simulations, accurately predicting the shape of the profiles and the *temperature slip* at the walls.

Cases 3-5 have isothermal walls with no imposed mean temperature gradients. Results for these cases are reported in Fig. 4. For Case 3, the four collision models provide similar predictions for the solids volume fraction and granular temperature profiles. It is worth noting that the value of the solids volume fraction in the QMOM calculations in Fig. 4(a) is slightly lower than in the MD simulations. This is due to finite-size effects, whose role is investigated in Section 6.7. For Case 4, the collision models all predict similar values of the solids volume fraction, as shown in Fig. 4(c), with the Boltzmann models predicting a slight upturn near the walls. The BGK model predicts very closely the tem-

---

[§]The 8-node quadrature formulation allows fourteen of the twenty transported moments to be controlled [18].

(a) Case 1, α_s

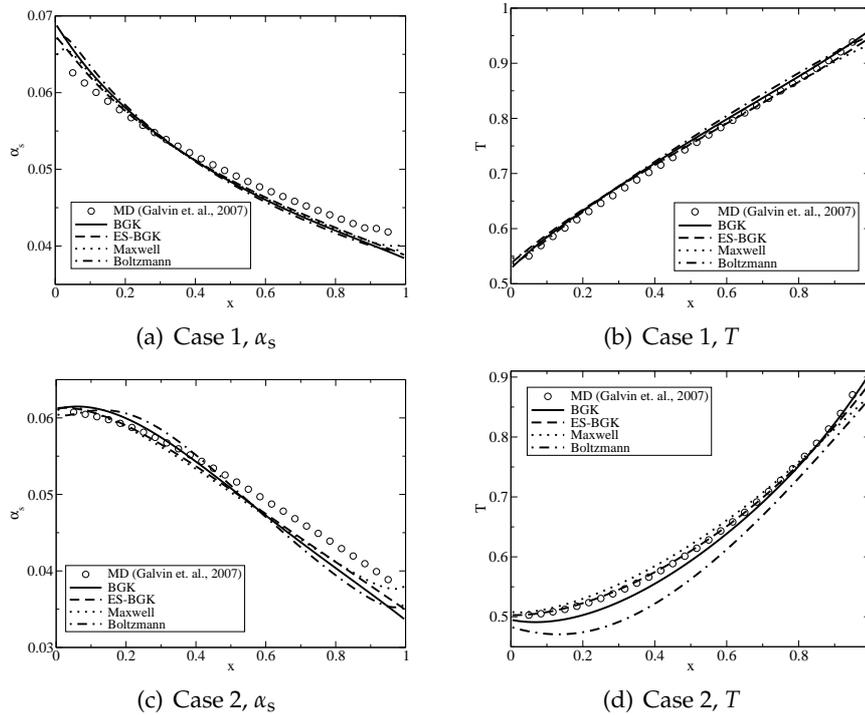(b) Case 1, T

(c) Case 2, α_s

(d) Case 2, T

Figure 3: Solids volume fraction and granular temperature profiles for cases with an imposed mean temperature gradient predicted by QMOM calculations with the four collision models.

perature profile for Case 4, as shown in Fig. 4(d). The full Boltzmann model generally underpredicts the temperature and has a flatter profile. For Case 4, the ES-BGK model provides results similar to BGK, while the inelastic Maxwell model overpredicts temperature near the center of the domain. In Case 5, the degree of in-elasticity of collisions between particles is further increased by lowering the restitution coefficient to $e = 0.9$. As shown in Fig. 4(e), the BGK model better predicts the maximum in the solids volume fraction, while the other models predict much flatter profiles. As shown in Fig. 4(f), the inelastic Maxwell model properly predicts the granular temperature trend near the walls, but it overpredicts the temperature values at the center of the channel. Granular temperature values are systematically under-predicted by the full Boltzmann model, especially near the walls. In comparison, the BGK model yields very good predictions of the temperature profile and accurately captures the "temperature slip" at the walls for all cases. In Case 5, all collision models overpredict the temperature at the center of the channel. This suggests that the model for the collision time τ used in the linearized models, which is exact in the limit $e = 1$, could be improved by including a weak dependence on e. More precisely, if τ were smaller for decreasing e, then the temperature at the center of channel would be lower when $e < 1$.

Alternatively, the over-prediction of the granular temperature near the centerline in the QMOM calculations consistently observed in Cases 3-5 might be explained by con-

(a) Case 3, α_s

(b) Case 3, T

(c) Case 4, α_s

(d) Case 4, T

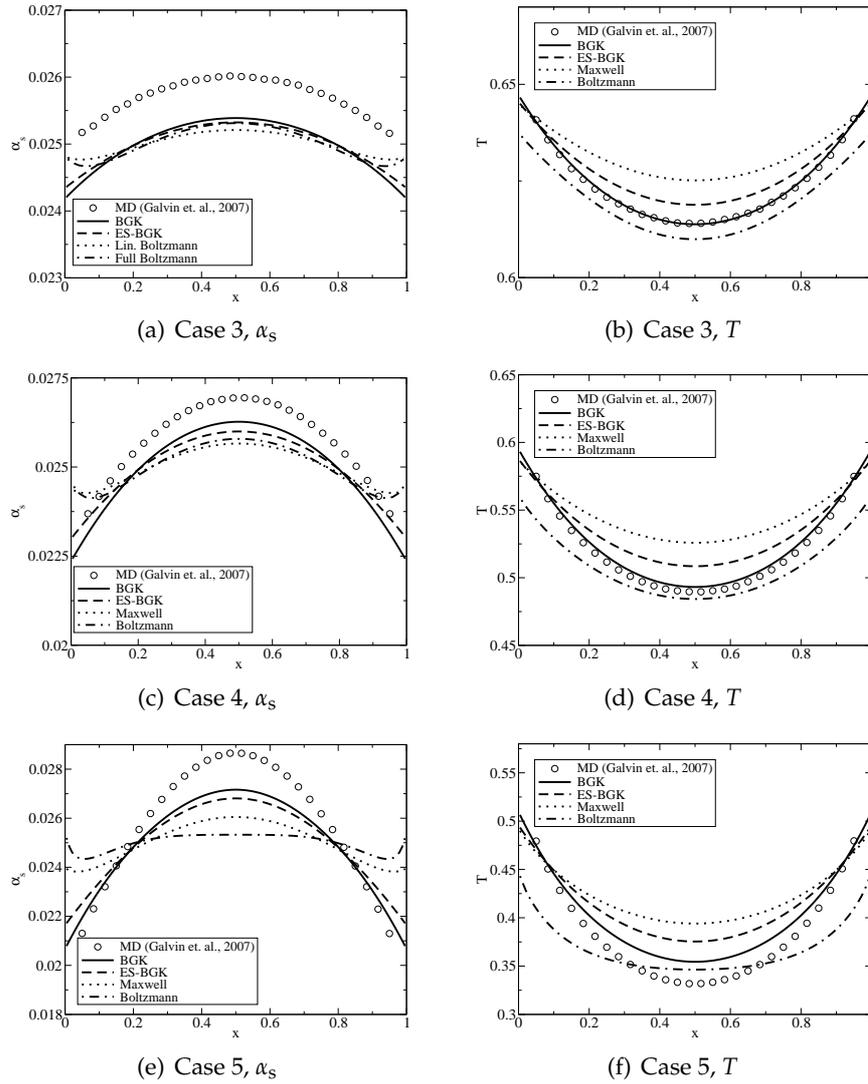(e) Case 5, α_s

(f) Case 5, T

Figure 4: Volume fraction and granular temperature profiles for cases with isothermal walls predicted by QMOM calculations with the four collision models.

sidering that the collision frequency predicted by the Boltzmann kinetic equation (and hence the temperature dissipation rate) is lower than in the MD simulations, due to the lack of consideration of finite-size effects (see Section 6.7). It is also worth noting that, as discussed in more detail below, the standardized central moments become more and more non-Gaussian as e decreases, with values for even-order central moments that are larger than the Gaussian values. Unlike with the BGK and ES-BGK models, in the two Boltzmann collision models, the values of all moments affect the collision term for any given moment through the values of the weights and abscissas. Thus, the two Boltzmann collision models will be more sensitive to the shape of the velocity distribution function

(and hence the values of the moments) than the other two collision models.

In general, in order to capture highly non-Gaussian behavior with a moment method, it is necessary to include a larger set of moments. In the quadrature-based moment method using the moment-inversion algorithm described in Section 3, highly non-Gaussian moments can result in negative weights if more than eight quadrature nodes are employed. For 64-node quadrature and moderate Kn, negative weights begin to occur for $e < 0.9$ for this system (the exact value of e depends on the collision model). Thus, in order to go to smaller values of e, the moment-inversion algorithm would need to be modified to eliminate the negative weights [39].

6.3 Temperature-component predictions

The model predictions for the granular temperature components are shown in Fig. 5 for Case 5, the case for which the differences between components is largest. In general, the QMOM calculations predict that the component in the wall-normal direction (T_1) is flatter than the other components. In comparison, the MD simulations show very small differences between the two components. In the QMOM calculations, the components T_1 and T_2 are equal a short distance from the wall, while at the centerline T_1 is slightly larger than T_2. This effect is less evident for the BGK results, which are closest to the MD simulations. In contrast, the full Boltzmann model predicts that T_1 is almost flat.
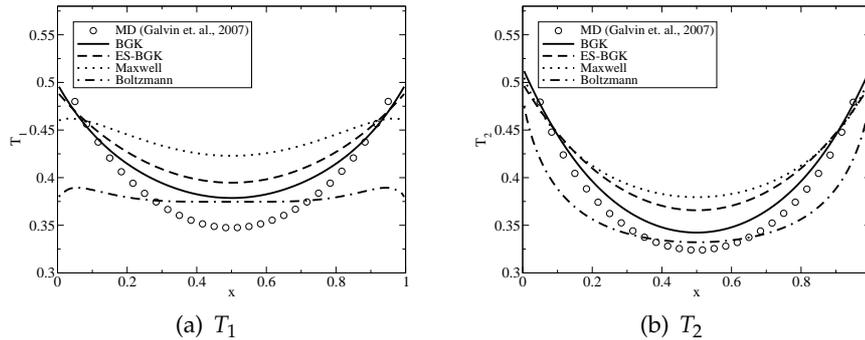

Figure 5: Granular temperature components predicted by QMOM calculations with the four collision models in Case 5.

6.4 Stress-tensor predictions

Stress-tensor components predicted by QMOM calculations are compared with MD results in this section. The stress-tensor components σ_{22} and σ_{33} are equal, as a consequence only the first one is reported in the figures. Likewise, as noted earlier, for this system with no mean velocity gradients the off-diagonal components of the stress tensor are null. For the MD results, three curves are plotted in Fig. 6, corresponding to the total stress and its two components due to kinetic and collisional-flux contributions. As noted earlier,

(a) Case 2, σ_{11}

(b) Case 2, σ_{22}

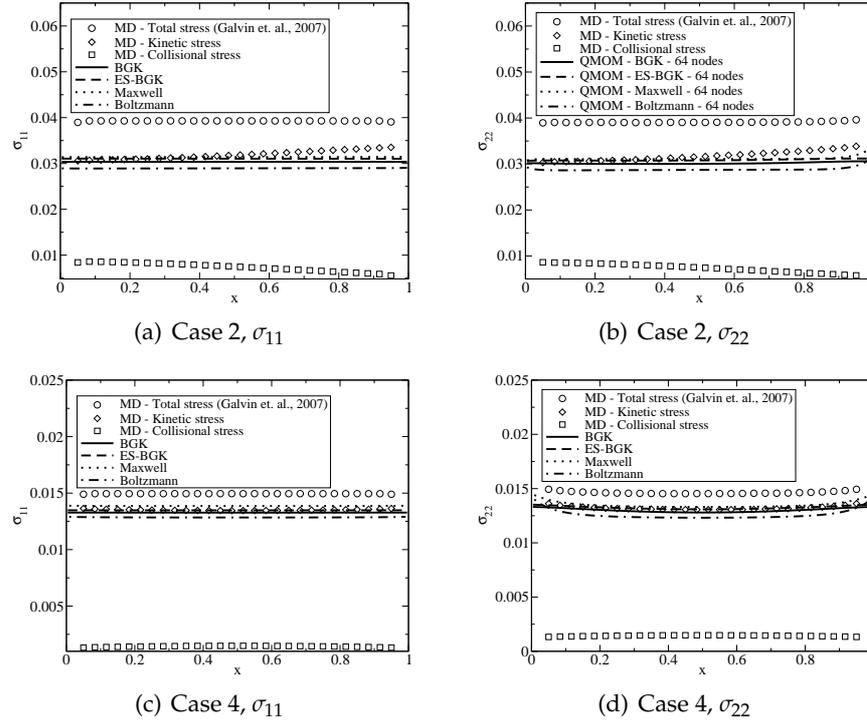(c) Case 4, σ_{11}

(d) Case 4, σ_{22}

Figure 6: Stress-tensor components in Cases 2 and 4 predicted by QMOM calculations with the four collision models. MD results for the total stress and the kinetic and collisional-flux contributions are shown separately.

the collisional-flux contribution is a finite-size effect that is not included in the QMOM calculations. Nevertheless, in all cases the QMOM calculations do remarkably well in predicting the kinetic contribution to the stress tensor. This observation is not completely unexpected. Indeed, all the moments sets used for quadrature include the second-order velocity moments, and all collision models provide a (nearly) exact description of the changes in the second-order moments due to collisions.

In Figs. 6(a) and 6(c) it can be observed that the total stress component in the wall-normal direction is constant (at steady state). This property follows directly from the moment transport equations for the zero- and first-order moments in the x_1 direction, written removing the unsteady term:

$$\frac{dM_{100}^1}{dx_1} = 0, \tag{6.1a}$$

$$\frac{dM_{200}^2}{dx_1} = 0. \tag{6.1b}$$

From (6.1a), it follows that M_{100}^1 is zero, because the walls are assumed to be impermeable to the particles, leading to a zero particle flux through the boundaries. From (6.1b), M_{200}^2 has to be constant. As a consequence, by considering the definition of σ_{11} in terms of the

moments:

$$\sigma_{11} = M^2_{200} - \alpha_s \left(\frac{M^1_{100}}{\alpha_s} \right)^2, \qquad (6.2)$$

the first term is constant, and the second term is zero, leading to the conclusion that σ_{11} must be constant. In general, Eq. (6.1b) will contain the total stress component in the wall-normal direction, hence, it will be constant even when the collisional-flux contribution is included. This fact can be observed for the MD results appearing in Fig. 6. It is worth noting that similar considerations cannot be applied for σ_{22}, because M^2_{020} does not produce a flux.

For all four collision models, the results for Case 1 (not shown) with $e=1$ yield $\sigma_{11} \approx \sigma_{22} \approx 0.036$, which agrees with the MD results for the kinetic stress, while the MD results for the total stress are $\sigma_{11} \approx \sigma_{22} \approx 0.046$. For the solids volume fraction used in Case 1, the collisional-flux contributes approximately 15 % of the total stress. The same is true for Case 2, where the stress-tensor components are shown in Fig. 6. As in Case 1, both components of the total stress are nearly constant, but now there are some differences between the four collision models. In general, the three linearized models (BGK, ES-BGK, inelastic Maxwell) yield the closest prediction of the kinetic stresses found from the MD simulations. Also, the fact that the three linearized models predict nearly the same kinetic stresses is not surprising since the collision terms for the second-order moments are exactly the same (see Appendix B).

The results for stress components for Case 4 are also shown in Fig. 6. In addition to the finite-size effects, it can be observed that with $e=0.96$ the two total stress components are distinctly different for the collision models and the MD results. As expected, σ_{11} is constant, but now σ_{22} exhibits a minimum at the centerline of the domain. In general, although the four collision models yield slightly different predictions for the kinetic stresses, the QMOM calculations are in very good agreement with the MD results in all cases.

Note that if our main objective was to reproduce the total stress, the QMOM results for the diagonal stress components could be increased by decreasing the collision frequency (the effective viscosity is proportional to the Knudsen number [35]). However, such a modification would also change the heat flux and, indirectly, the solids volume fraction and temperature profiles. Overall, we can conclude that even without the collisional-flux contributions due to finite-size particles the zero-order kinetic model should be adequate to model dilute granular flows with solids volume fractions less than approximately 2-4%.

6.5 Heat-flux predictions

It is well known in kinetic modeling that correctly capturing the heat flux is an important, yet difficult requirement to meet for finite Knudsen numbers [23], mainly because as a third-order moment it depends on fourth- and higher-order moments that are difficult to close. Predicting the heat flux correctly is, however, important for the overall model
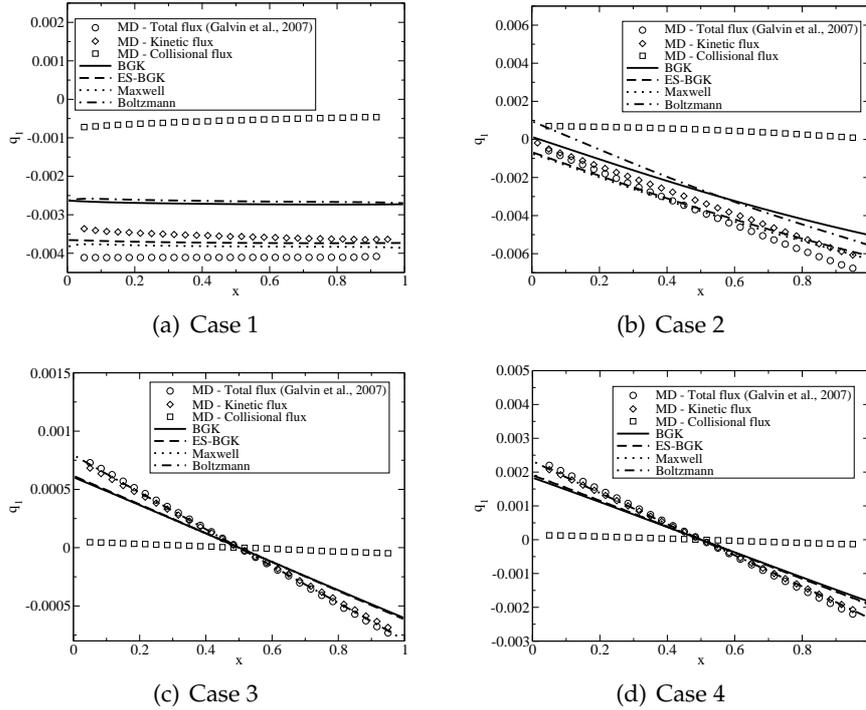
Figure 7: Heat flux profiles in Cases 1-4 predicted by QMOM calculations with the four collision models. MD results for the total heat flux and the kinetic and collisional-flux contributions are shown separately.

since it determines the granular temperature distribution, which in turn has a strong influence on the solids volume fraction profiles. As seen earlier, the 64-node quadrature-based moment method has generally good predictions for the solids volume fraction and granular temperature profiles. We can thus anticipate that the heat-flux predictions must be in relatively good agreement with the MD data. The collisional-flux contribution to the heat flux in the MD results is relatively small (see Fig. 7); hence we will mainly discuss the comparison between the QMOM and MD results for the kinetic part of the heat flux.

In Cases 1 and 2, a mean temperature gradient is imposed on the granular flow. For Case 1 the predicted profiles of the heat flux are shown in Fig. 7(a). For this case, due to conservation of energy when $e=1$, the total heat flux must be constant at steady state.[¶] The ES-BGK and inelastic Maxwell models provide results in good agreement with the MD data. As expected, due to the larger Prandtl number, the BGK model predicts a smaller (in magnitude) heat flux than the ES-BGK model. It is noteworthy that heat flux predicted by the full Boltzmann model, even though in theory should be more accurate,

---

[¶]In general, it is easily shown that at steady state $\partial_1 q_1 = (C_{200}^2 + 2C_{020}^2)/2$. The second-order moments of the collision term and a boundary condition thus determine the kinetic heat flux. By symmetry, when $T_C = T_H$, $q_1(1/2)=0$. From kinetic theory, $\partial_1 q_1 \approx -\gamma_T T^{3/2}$, with temperature dependence being exact for the linearized collision models. From the MD data and the model, at steady state the temperature dissipation is nearly constant, consistent with the observed weak variation in T.

is almost the same as the heat flux predicted by the BGK model. For Case 2, the ES-BGK and inelastic Maxwell models predict values of the heat flux (Fig. 7(b)) close to the MD results, while the full Boltzmann and BGK models results are slightly farther from the MD results. The differences observed in Case 2 between the BGK and ES-BGK models can be again attributed to the difference in the Prandtl numbers predicted by the two models.

In Cases 3 and 4, the walls are isothermal and the temperature gradients are created by inelastic collisions. For both cases, the three linearized models predict essentially the same heat flux, while the full Boltzmann model is closest to the MD results (see Figs. 7(c) and 7(d)). For Case 5 (not shown), the accuracy of the heat flux predictions are very similar to Cases 3 and 4. Note that for the cases with isothermal walls, the collisional-flux contribution to the heat flux is very small relative to the kinetic contribution.

Overall, the model predictions for the heat flux in all cases considered are remarkably good. It is worth noting that unlike in "standard" hydrodynamic models for granular systems [6, 24–26, 29, 30] that require a constitutive equation for the stress tensor and the heat flux (as well as consistent boundary conditions for the solids volume fraction, mean velocity and temperature), the quadrature-based moment closure is fully self contained and self consistent. The principle factor (besides the level of quadrature) that determines the accuracy of a moment model is the degree to which the starting kinetic equation (2.1) and the collision model describes the system. Based on the observed agreement between the QMOM and MD simulation results, we can conclude that the Boltzmann kinetic equation with a zero-order collision model is adequate to capture Knudsen number effects in dilute granular flows.

6.6   Non-Gaussian moments due to inelastic collisions

It is well known [8] that in the homogeneous cooling state the velocity moments of a granular flow show small deviations from the Gaussian values for $e < 1$. In comparison, for the system studied in this work, the inelastic collisions generate moments that are much farther from the Gaussian values due to the presence of the mean temperature gradients. To illustrate how significant is the non-Gaussian behavior, we present results for selected standardized central moments for Case 5 ($e = 0.9$). In the homogeneous case (see Appendix C and [8]) the odd-order moments are null. In Fig. 8 two odd-order moments Q_{300}^{3} and Q_{500}^{5} are compared with the Gaussian values of zero for the four collision models. From these plots, it is obvious that the underlying velocity distribution function is highly skewed along the v_1 direction with the largest skewness near the walls, changing signs at the centerline. The corresponding odd central moments are zero in the v_2 and v_3 directions. The three linearized collision models predict approximately the same degree of skewness, while for the full Boltzmann model it is considerably larger. Overall, we can conclude that the odd-order moments are non-zero due to the mean temperature gradient in the x_1 direction generated by inelastic collisions.

In Fig. 8, a selected set of even-order central moments (Q_{400}^{4}, Q_{040}^{4}, Q_{600}^{6}, Q_{060}^{6}) are
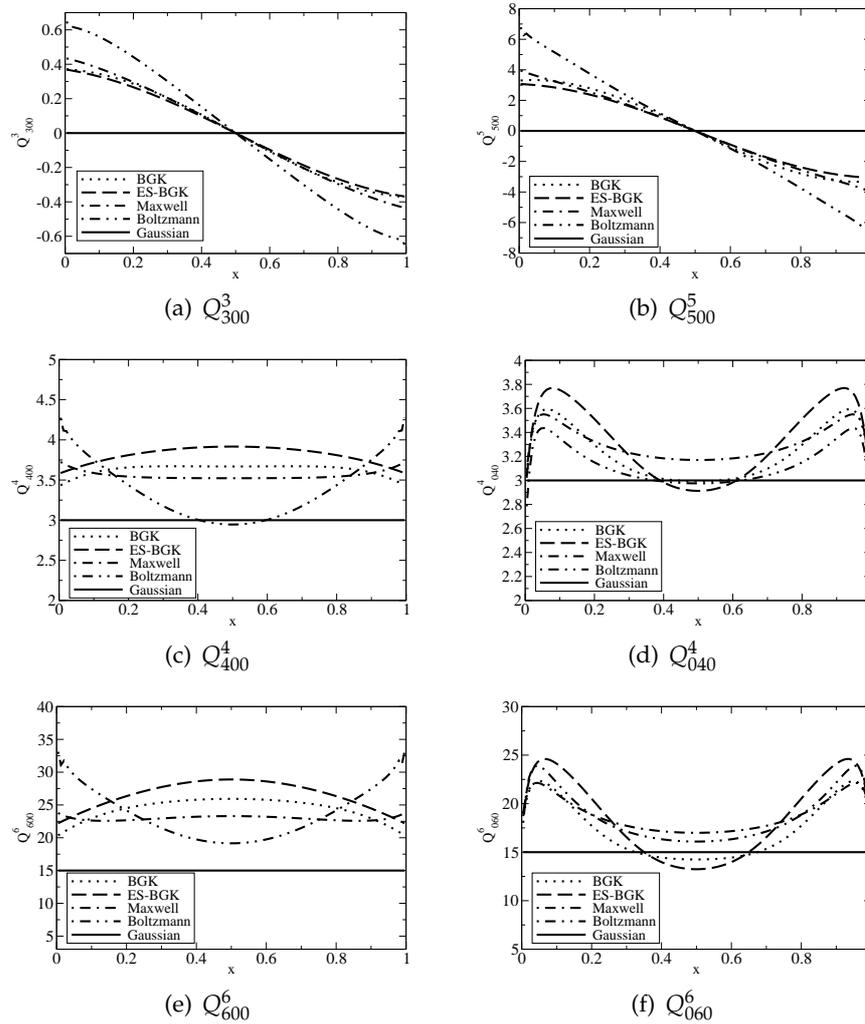
Figure 8: Standardized central moments predicted by QMOM calculations with the four collision models in case 5. Gaussian values are shown by the dashed lines.

compared with their Gaussian values. As can be clearly observed, the even-order central moments have values near the walls that are much larger than the Gaussian values. For the even-order moments of the velocity component in the direction of the mean temperature gradient (v_1), the BGK and ES-BGK results are largest at the centerline and smallest at the walls. The opposite trend is observed for the two Boltzmann models, with the full Boltzmann model predicting sub-Gaussian moments at the center of the domain. For the even-order moments of the velocity component in the other direction (v_2), the results for all collision models are lower at the centerline and peak near the walls. It is noteworthy that the wall-normal velocity components are not Gaussian at the walls for any of the collision models, even though the wall boundary condition is Gaussian. This is caused

by "moment slip" due to the finite Knudsen number of the flow. The non-Gaussian behavior is absent for $e=1$, and increases rapidly with decreasing e. In principal, because they include terms for all of the moments, the two Boltzmann models should be more accurate for moments shown in Fig. 8, and the full Boltzmann model should be more accurate than the inelastic Maxwell model.

6.7   A simple correction for finite-size effects

The collision models considered in this work assumes particles to have zero effective volume during wall collisions, while the MD simulation considers finite-size particles. Finite-size effects at the walls are responsible for the lower value of the solids volume fraction predicted by QMOM calculations, for example in Case 4 (Fig. 4(c)). In [23], the ratio between the channel width L and the particle diameter d_p is set to 35, as a consequence the center of a particle can be at a minimum distance from the wall equal to $d_p/2$. For point particles where all of the particle volume is assigned to the center point, this is equivalent to considering a system with a dimensionless length of $1-d_p/L=0.972$. Since the total volume of the particle phase is fixed ($L\bar{\alpha}$ is constant), the effective average solids volume fraction in the MD simulations is thus equal to $\alpha_{s,eq}=\bar{\alpha}/(1-d_p/L)$, which, for Cases 3-5, is $\alpha_{s,eq}=0.0257$.

In order to examine whether correcting the solids volume fraction has a significant effect on the results, Case 4 was run again using $\alpha_s=0.0257$ and $L=0.972$ with the BGK collision model. Fig. 9(a) shows that, with the corrected value of the initial solids volume fraction, excellent agreement with the MD data for the solids volume fraction profile is obtained. The higher value of the solids volume fraction has only a small effect on the temperature profiles shown in Fig. 9(b). The stress-tensor components (Fig. 9(c)) exhibit only very small differences with respect to the QMOM prediction with the original value of average solids volume fraction. Likewise, the heat flux (Fig. 9(d)) shows only a small change in slope. Overall, we can conclude that correcting only for the effective solids volume fraction is adequate to capture the solids volume fraction profiles. However, a first-order collision model that accounts for finite-size particles during collisions [22] (see Appendix A) would be required for further improvements in the QMOM predictions for the stress tensor.

7   Conclusions

A kinetic model using high-order quadrature-based moment methods was applied to simulate a dilute non-isothermal granular flow bounded between two parallel walls. Three different orders of approximation were considered by using 8-, 27-, and 64-node quadrature. Quadrature-based closures were provided for the spatial fluxes of the moments and four different collision models were investigated. The accuracy of the kinetic model was validated using MD simulations of a nearly equivalent system.
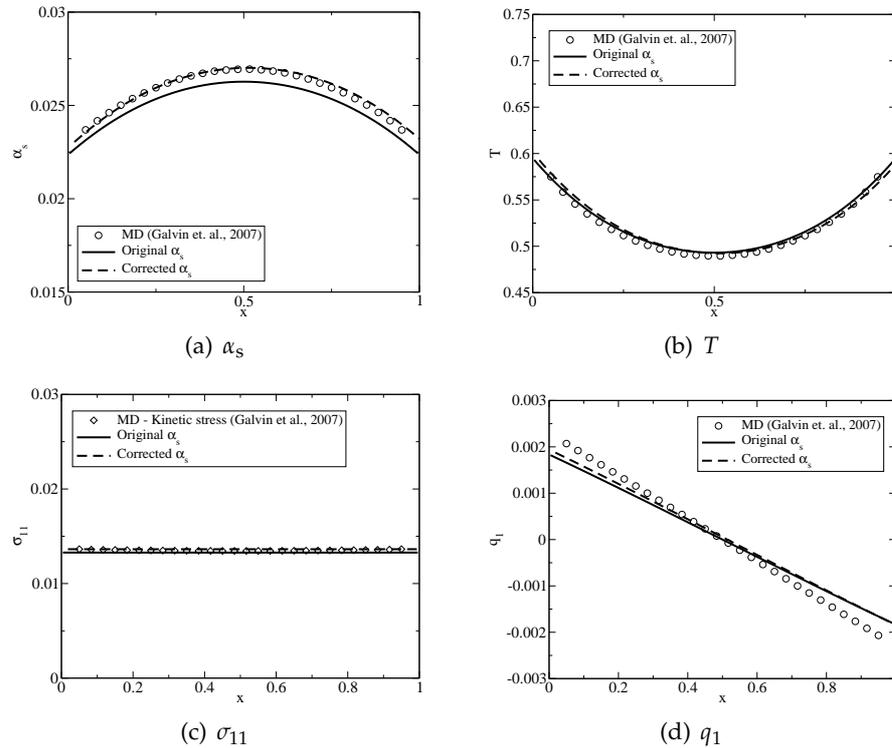
Figure 9: Profiles predicted by QMOM calculations with the BGK model in Case 4 with the original ($\alpha_s = 0.025$) and corrected ($\alpha_s = 0.0257$) values of the initial solids volume fraction.

First, the accuracy of the quadrature closures was determined as a function of the number of quadrature nodes, showing that the 8-node quadrature provides limited accuracy for all cases, but especially for cases with inelastic collisions. The reason of this behavior was identified as the inadequate representation of the spatial fluxes with 8-node quadrature, in agreement with previous work for other systems [19]. However, it was shown that higher-order quadrature methods are not affected by this problem, and provide satisfactory results for all cases investigated.

Next, comparison of the inelastic collision models showed that all four models provided good results for all the cases considered. However, their predictive accuracy degrades when the restitution coefficient is decreased substantially. Surprisingly, use of the full Boltzmann collision model did not improve the accuracy of the predictions, despite its substantially higher computation cost. It is likely that this observation will not hold for other, more complex, granular flows (e.g., multi-component cases). In such cases, the inelastic Maxwell collision model may offer an attractive alternative to the simpler BGK-type models.

Finally, the kinetic model was shown to properly predict the kinetic part of the stress tensor, with a constant component in the wall-normal direction, and good agreement with the temperature components, related to the diagonal components of the stress ten-

sor. Differences in the predictions of QMOM and MD simulations can be explained by the fact that the zero-order collision models neglect finite-size effects present in the MD results. Since such effects were shown to be relatively small for the heat flux, the QMOM predictions for the heat flux were generally quite satisfactory. Overall, the quadrature-based moment method developed in this work appears to be well suited for dealing with finite-Knudsen-number effects in dilute granular flows.

In closing, we wish to emphasize that a key component of quadrature-based moment methods is the moment-inversion algorithm that related the weights and abscissas to the moments. In this work we have used the algorithm proposed in [19] that employs a tensor product of 1-D quadratures to define the abscissas. However, for some cases (e.g., infinite Knudsen number with walls at different temperatures), the tensor product formulation can be overly restrictive, leading to negative weights. In order to overcome this shortcoming, we have recently developed less restrictive moment-inversion algorithms using conditional moments [39] based on the "optimal" moments sets reported in [20], for which non-negative weights are guaranteed for any optimal set of realizable moments. Results using this *conditional* quadrature method of moments (CQMOM) will be reported elsewhere.

Acknowledgments

A   Boltzmann-Enskog collision integral

For inelastic hard-sphere collisions, the Boltzmann-Enskog collision integral [14] is defined as

$$\mathbb{C} = \frac{6}{\pi d_p} \int_{\mathbb{R}3} \int_{\mathbf{S}^+} \left[\chi f^{(2)}(\mathbf{x}, \mathbf{v}_1''; \mathbf{x} - d_\mathrm{p}\mathbf{n}, \mathbf{v}_2'') - f^{(2)}(\mathbf{x}, \mathbf{v}_1; \mathbf{x} + d_\mathrm{p}\mathbf{n}, \mathbf{v}_2) \right] |\mathbf{g} \cdot \mathbf{n}| \mathrm{d}\mathbf{n} \mathrm{d}\mathbf{v}_2, \qquad \text{(A.1)}$$

where $f^{(2)}$ is the pair correlation function, $\mathbf{n} = (\mathbf{x}_1 - \mathbf{x}_2)/|\mathbf{x}_1 - \mathbf{x}_2|$ is the unit vector in the direction between the particle centers, $\mathbf{g} = \mathbf{v}_1 - \mathbf{v}_2$ (with magnitude g) is the velocity difference before a direct collision, and χ is a factor relating the pre-collision velocities for direct collisions $(\mathbf{v}_1, \mathbf{v}_2)$ to those for inverse collisions $(\mathbf{v}_1'', \mathbf{v}_2'')$. These velocities are related by [12, 14]

$$\mathbf{v}_1 = \mathbf{v}_1'' - \omega(\mathbf{g}'' \cdot \mathbf{n})\mathbf{n}, \qquad \text{(A.2)}$$
$$\mathbf{v}_2 = \mathbf{v}_2'' + \omega(\mathbf{g}'' \cdot \mathbf{n})\mathbf{n}, \qquad \text{(A.3)}$$

where $\omega = (1+e)/2$ and $0 \leq e \leq 1$ is the coefficient of restitution, and $\mathbf{g}'' = \mathbf{v}_1'' - \mathbf{v}_2''$ is the velocity difference before an inverse collision. The surface S^+ is the unit half sphere on which $\mathbf{g} \cdot \mathbf{n} > 0$ (i.e., velocity differences that result in collisions).

Starting from Eq. (A.1), the source term for the moments [22] can be written as

$$C_{ijk}^{\gamma} = \frac{6}{\pi d_{\mathrm{p}}} \int_{\mathbb{R}3} \int_{\mathbb{R}3} \int_{\mathsf{S}^+} \left[(v_{1,1}')^i (v_{1,2}')^j (v_{1,3}')^k - (v_{1,1})^i (v_{1,2})^j (v_{1,3})^k \right]$$
$$f^{(2)}(\mathbf{x}, \mathbf{v}_1; \mathbf{x} + d_{\mathrm{p}} \mathbf{n}, \mathbf{v}_2) |\mathbf{g} \cdot \mathbf{n}| \mathrm{d}\mathbf{n} \mathrm{d}\mathbf{v}_1 \mathrm{d}\mathbf{v}_2, \tag{A.4}$$

where $\mathbf{v}'$ denotes velocity vectors after a direct collision. The pair correlation function at contact is approximated by

$$f^{(2)} \left(\mathbf{x} - \frac{d_{\mathrm{p}}}{2} \mathbf{n}, \mathbf{v}_1; \mathbf{x} + \frac{d_{\mathrm{p}}}{2} \mathbf{n}, \mathbf{v}_2 \right) = g_0 f_1(\mathbf{v}_1) f_2(\mathbf{v}_2) \left(1 + \frac{d_{\mathrm{p}}}{2} \mathbf{n} \cdot \boldsymbol{\nabla} \ln D \right) + \mathcal{O}((d_{\mathrm{p}}/L)^2), \tag{A.5}$$

where $g_0(\alpha_{\mathrm{s}})$ is the radial distribution function depending on the solids volume fraction $\alpha_{\mathrm{s}} = M^0$, and $D = \ln(f(\mathbf{v}_2)/f(\mathbf{v}_1))$. Neglecting gradients in g_0, expansion about the point of contact and rearrangement of the terms on the right-hand side of Eq. (A.4) leads to

$$C_{ijk}^{\gamma} = C_{ijk} + \frac{d_{\mathrm{p}}}{2} \boldsymbol{\nabla} \cdot \mathbf{G}_{ijk} + \mathcal{O}((d_{\mathrm{p}}/L)^2), \tag{A.6}$$

where the collision contribution is defined by

$$C_{ijk} = \frac{6g_0}{d_{\mathrm{p}}} \int_{R^3} \int_{R^3} g I_{ijk}(\omega, \mathbf{v}_1, \mathbf{g}) f(\mathbf{v}_1) f(\mathbf{v}_2) \mathrm{d}\mathbf{v}_1 \mathrm{d}\mathbf{v}_2, \tag{A.7}$$

and the collisional-flux contribution by

$$\mathbf{G}_{ijk} = \frac{6g_0}{d_{\mathrm{p}}} \int_{\mathbb{R}^3} \int_{\mathbb{R}^3} g \mathbf{F}_{l_1 l_2 l_3}(\omega, \mathbf{v}_1, \mathbf{g}) f(\mathbf{v}_1) f(\mathbf{v}_2) \mathrm{d}\mathbf{v}_1 \mathrm{d}\mathbf{v}_2. \tag{A.8}$$

Up to first order in d_{p}/L, I_{ijk} in Eq. (A.7) is defined by

$$I_{ijk} = \frac{1}{\pi g} \int_{\mathsf{S}^+} \left[(v_{1,1}')^i (v_{1,2}')^j (v_{1,3}')^k - v_{1,1}^i v_{1,2}^j v_{1,3}^k \right] |\mathbf{g} \cdot \mathbf{n}| \left(1 + \frac{d_{\mathrm{p}}}{2} \mathbf{n} \cdot \boldsymbol{\nabla} D \right) \mathrm{d}\mathbf{n}, \tag{A.9}$$

and $\mathbf{F}_{ijk}$ in Eq. (A.8) by

$$\mathbf{F}_{ijk} = \frac{1}{\pi g} \int_{\mathsf{S}^+} \mathbf{n} \left[(v_{1,1}')^i (v_{1,2}')^j (v_{1,3}')^k - v_{1,1}^i v_{1,2}^j v_{1,3}^k \right] |\mathbf{g} \cdot \mathbf{n}| \left(1 + \frac{d_{\mathrm{p}}}{2} \mathbf{n} \cdot \boldsymbol{\nabla} D \right) \mathrm{d}\mathbf{n}. \tag{A.10}$$

Note that the collisional-flux term in Eq. (A.6) is first order in d_{p}/L, and thus is neglected in a zero-order collision model.

In the main text, a zero-order approximation is used to represent the collisions. The moment source term due to collisions is thus

$$C_{ijk}^{\gamma} = \frac{6g_0}{d_{\rm p}} \int_{R^3} \int_{R^3} g I_{ijk}(\omega, \mathbf{v}_1, \mathbf{g}) f(\mathbf{v}_1) f(\mathbf{v}_2) \mathrm{d}\mathbf{v}_1 \mathrm{d}\mathbf{v}_2, \tag{A.11}$$

with

$$I_{ijk} = \frac{1}{\pi g} \int_{\rm S^+} \left[(v'_{1,1})^i (v'_{1,2})^j (v'_{1,3})^k - v_{1,1}^i v_{1,2}^j v_{1,3}^k \right] |\mathbf{g} \cdot \mathbf{n}| \mathrm{d}\mathbf{n}. \tag{A.12}$$

As discussed in the main text, the integral on the right-hand side of Eq. (A.12) can be evaluated explicitly, and Eq. (A.11) can be evaluated using quadrature. The kinetic model given by Eq. (A.11) is referred to in the main text as the full Boltzmann collision model.

B   Kinetic models for granular flow

For elastic collision, several different kinetic models have been proposed to close the Boltzmann hard-sphere collision term [13, 35]. For inelastic collisions ($e < 1$), one must correctly account for the dependence of dissipation of granular energy on the value of e. One method for accomplishing this task is to start from the exact (unclosed) collision integral in Eq. (A.11). From the definition of I_{ijk} given in Eq. (A.12), it can be shown that

$$C_{ijk}^{*\gamma} = \frac{6g_0 \langle g \rangle}{d_{\rm p}} \int_{\mathbb{R}^3} \int_{\mathbb{R}^3} I_{ijk}(\omega, \mathbf{v}_1, \mathbf{g}) f(\mathbf{v}_1) f(\mathbf{v}_2) \mathrm{d}\mathbf{v}_1 \mathrm{d}\mathbf{v}_2 \tag{B.1}$$

is closed in terms of the moments up to order γ. The mean velocity difference is defined by

$$\langle g \rangle = \frac{1}{\alpha_{\rm s}^2} \int_{\mathbb{R}^3} \int_{\mathbb{R}^3} |\mathbf{v}_1 - \mathbf{v}_2| f(\mathbf{v}_1) f(\mathbf{v}_2) \mathrm{d}\mathbf{v}_1 \mathrm{d}\mathbf{v}_2, \tag{B.2}$$

and the integrals on the right-hand side of Eq. (B.2) can be evaluated using quadrature. However, at equilibrium, it is straightforward to show that $\langle g \rangle = 4\sqrt{T/\pi}$. Note that Eq. (B.1) corresponds to an inelastic Maxwell particle with $B = \langle g \rangle \mathbf{g} \cdot \mathbf{n}/g$, (see [32]), and, most importantly, it still contains the exact dependence on $\omega = (1+e)/2$. In the main text, the kinetic model given by Eq. (B.1) is referred to as the inelastic Maxwell collision model.

A simpler class of kinetic models has the form

$$\mathbb{C} = \frac{1}{\tau}(f^* - f), \tag{B.3}$$

where (repeated Roman indices imply summation)

$$f^* = \frac{\alpha_{\rm s}}{\left[\det(2\pi\lambda)\right]^{1/2}} \exp\left[-\frac{1}{2}(v_i - U_{\rm pi})(\lambda^{-1})_{ij}(v_j - U_{\rm pj}) \right], \tag{B.4}$$

$\mathbf{U}_\mathrm{p}$ is the mean particle velocity, and $\boldsymbol{\lambda}^{-1}$ is the inverse of the second-order tensor $\boldsymbol{\lambda}$, defined such that a given set of velocity moments agrees with Eq. (B.1). Due to conservation of mass and mean momentum, the first non-zero terms from Eq. (B.1) correspond to the second-order moments. Letting κ denote the symmetric second-order tensor constructed from I_{ijk} with $i+j+k=2$:

$$\kappa = \frac{\omega}{2}\left(\frac{\omega g^2}{6}\mathbf{I} + \frac{\omega}{2}\mathbf{g}\otimes\mathbf{g} - \mathbf{g}\otimes\mathbf{v}_1 - \mathbf{v}_1\otimes\mathbf{g}\right), \tag{B.5}$$

the collision term for the second-order moments is given by

$$C^{*2} = \frac{6g_0\langle g\rangle}{d_\mathrm{p}}\int_{\mathbb{R}^3}\int_{\mathbb{R}^3}\kappa(\mathbf{v}_1,\mathbf{v}_2)f(\mathbf{v}_1)f(\mathbf{v}_2)\mathrm{d}\mathbf{v}_1\mathrm{d}\mathbf{v}_2. \tag{B.6}$$

The integral on the right-hand side of this expression can be evaluated explicitly:

$$C^{*2} = \frac{6g_0\langle g\rangle\omega\alpha_\mathrm{s}^2}{d_\mathrm{p}}\left(\frac{\omega T}{2}\mathbf{I} + \frac{\omega}{2}\sigma - \sigma\right), \tag{B.7}$$

where σ is the velocity-covariance tensor and $T = \mathrm{tr}(\sigma)/3$. Using $\omega(\omega-1) = (e^2-1)/4$, it is straightforward to show that for this collision model the homogeneous granular temperature obeys

$$\frac{dT}{dt} = -\frac{3g_0\langle g\rangle\alpha_\mathrm{s}(1-e^2)}{2d_\mathrm{p}}T, \tag{B.8}$$

where $\langle g\rangle \approx 4\sqrt{T/\pi}$.

The collision term for the second-order moments found from Eq. (B.3) is

$$C^2 = \frac{\alpha_\mathrm{s}}{\tau}(\boldsymbol{\lambda} - \sigma). \tag{B.9}$$

Equating this expression to Eq. (B.7), we find that $\tau = \zeta d_\mathrm{p}/(3g_0\langle g\rangle\alpha_\mathrm{s})$ and

$$\boldsymbol{\lambda} = \zeta\omega^2 T\mathbf{I} + (\zeta\omega^2 - 2\zeta\omega + 1)\sigma, \tag{B.10}$$

where $0 < \zeta \le 3/2$ is a model constant. In the elastic limit ($\omega = 1$), Eq. (B.3) corresponds to the ES-BGK model with the Prandtl number given by $\mathrm{Pr} = 1/\zeta$, and to the BGK model when $\zeta = 1$. For inelastic collisions, we will refer to the BGK and ES-BGK models as Eq. (B.10) with the values of ζ used in the elastic limit. The only remaining unclosed term is $\langle g\rangle$. At equilibrium in the elastic limit, $\mathbf{g}$ will be Gaussian with zero mean and covariance $2T\mathbf{I}$. This fact leads to the approximation $\langle g\rangle = 4\sqrt{T/\pi}$, and thus we use $\tau = \zeta\sqrt{\pi}d_\mathrm{p}/(12g_0\alpha_\mathrm{s}\sqrt{T})$ in the main text.

C Quadrature-based closure of the full Boltzmann collision model

The moments of the velocity distribution function computed in the homogeneous case of mono-dispersed particles colliding without the effect of external forces can be computed by considering equation

$$\partial_t f = \mathbb{C}, \tag{C.1}$$

and by applying the quadrature method presented in Eq. (3.15) to evaluate the rate of change of f due to collisions. Note that the moments in the homogeneous case with $e < 1$ attain a self-similar state wherein the standardized moments are time invariant. If the calculation of the self-similar state is performed with the full Boltzmann collision model, the values reported in Table 2 are obtained for $N = 64$ and selected values of e, where the non-zero standardized, isotropic moments are reported and compared to the corresponding Gaussian values (recall that 64-node quadrature requires velocity moments up to seventh order). In comparison, for the homogeneous case the inelastic Maxwell collision model yields Gaussian moments with $e = 1$ and central moments slightly larger than Gaussian for $e < 1$.

Table 2: Non-zero standardized central moments found from the 64-node quadrature closure of the full Boltzmann collision model.

Moment	m_G	m_q ($e=1$)	E [%]	m_q ($e=0.99$)	m_q ($e=0.96$)	m_q ($e=0.9$)	m_q ($e=0$)
Q_{000}^0	1	1	0	1	1	1	1
Q_{200}^2	1	1	0	1	1	1	1
Q_{400}^4	3	2.904926	3.169	2.896908	2.876192	2.847585	2.473231
Q_{220}^4	1	0.998218	0.178	0.995885	0.990243	0.984455	1.125439
Q_{600}^6	15	15.32622	2.175	15.21579	14.95051	14.67770	18.85057
Q_{222}^6	1	0.995733	0.427	0.989091	0.973259	0.957705	1.485397

The relative error between the Gaussian and the quadrature-based values, defined by $E = |m_G - m_q|/m_G$, is reported in Table 2 for $e = 1$, where m_G is the moment of the Gaussian distribution and m_q is the value of the corresponding moment computed using the quadrature closure. The maximum observed error is 3.169% on the fourth-order moment m_{040}. The deviations from the Gaussian moments exhibit a weak dependence on e, first becoming more sub-Gaussian as e decreases from unity but then becoming super-Gaussian for e near zero. The behavior near $e = 1$ is consistent with the known results for the homogeneous cooling state of a granular flow [8]. Nevertheless, the sixth-order central moment with $e = 0$ is considerably smaller than the corresponding central moment for Case 5 with $e = 0.9$ in the main text, indicating that the presence of a mean temperature gradient has a much stronger effect on the non-Gaussian behavior than does the restitution coefficient.

It is worth noting that the deviation of the moments predicted by QMOM in the case $e = 1$ from the Gaussian value is a result of the discretization error introduced by the

quadrature representation of the distribution function used to close the collision integral. As discussed in the main text, the continuum distribution function is approximated by a finite set of Dirac delta function, in number equal to the number of quadrature weights. The accuracy of this approximation depends on the number of quadrature nodes, and on the shape of the distribution function to be approximated. In particular, the accuracy of the quadrature representation of the distribution increases with the number of quadrature nodes.

D   The moment-inversion algorithm

The moment-inversion algorithm is key to the quadrature-based moment method, because it allows the weights and abscissas to be found from the moments. The procedure is summarized here for the case of third-order quadrature using eight nodes, in order to give the reader the foundation behind the construction of the quadrature formula; however, a detailed explanation of higher-order quadrature can be found elsewhere [19]. Recently, a novel moment-inversion algorithm has been developed [39] that guarantees non-negative weights for realizable sets of higher-order moments. Preliminary computations suggest that increased accuracy can be obtained with the new algorithm for a given number of quadrature nodes [39], but otherwise the results are consistent with those presented in the main text.

The moment-inversion algorithm used in this work [19] is defined in terms of the rotated central moments R_{ijk}^{γ}, obtained from the moments M_{ijk}^{γ} with a linear transformation **L**. The moments are translated with respect to the mean velocity and rotated to diagonalize the velocity covariance matrix. Letting $\mathbf{U}_{\mathrm{p}}$ denote the mean particle velocity vector, and σ_U the velocity covariance matrix, we introduce the vector

$$\mathbf{X} = \mathbf{L}^{-1}(\mathbf{v} - \mathbf{U}_{\mathrm{p}}),$$

where **L** is the upper Cholesky decomposition of σ_U (see [18]).

For third-order quadrature, weights and abscissas in each direction are found by applying the two-node quadrature formulas [27, 37] to the three sets of rotated moments with respect to the principal directions:

$$\rho_{i1} = \frac{1}{2} + \xi_i, \qquad X_{i1} = -\sqrt{\frac{1 - 2\xi_i}{1 + 2\xi_i}}, \tag{D.1}$$

$$\rho_{i2} = \frac{1}{2} - \xi_i, \qquad X_{i2} = +\sqrt{\frac{1 + 2\xi_i}{1 - 2\xi_i}}, \tag{D.2}$$

where

$$\xi_i = \frac{m_i^3}{2\sqrt{4 + (m_i^3)^2}}. \tag{D.3}$$

This operation provides the univariate sets of weights and abscissas:

$$\{\rho_{11}, X_{11}; \rho_{12}, X_{12}\}, \qquad \{\rho_{21}, X_{21}; \rho_{22}, X_{22}\}, \qquad \{\rho_{31}, X_{31}; \rho_{32}, X_{32}\}. \qquad \text{(D.4)}$$

The three-dimensional quadrature approximation is defined using the tensor product of the univariate abscissas, leading to the definition of the following set of weights and abscissas:

$$\begin{aligned}
\big[(\rho_1^*, X_{11}, X_{21}, X_{31}), (\rho_2^*, X_{12}, X_{21}, X_{31}), \ (\rho_3^*, X_{11}, X_{22}, X_{31}), (\rho_4^*, X_{12}, X_{22}, X_{31}), \\
(\rho_5^*, X_{11}, X_{21}, X_{32}), (\rho_6^*, X_{12}, X_{21}, X_{32}), \ (\rho_7^*, X_{11}, X_{22}, X_{32}), (\rho_8^*, X_{12}, X_{22}, X_{32})\big].
\end{aligned} \qquad \text{(D.5)}$$

The weights ρ_i^* are determined by constraints consistent with the univariate nodes, by solving a linear system of equations:

$$\rho_1^* + \rho_3^* + \rho_5^* + \rho_7^* = \rho_{11}, \quad \rho_2^* + \rho_4^* + \rho_6^* + \rho_8^* = \rho_{12}, \quad \rho_1^* + \rho_2^* + \rho_5^* + \rho_6^* = \rho_{21}, \qquad \text{(D.6)}$$

$$\rho_3^* + \rho_4^* + \rho_7^* + \rho_8^* = \rho_{22}, \quad \rho_1^* + \rho_2^* + \rho_3^* + \rho_4^* = \rho_{31}, \quad \rho_5^* + \rho_6^* + \rho_7^* + \rho_8^* = \rho_{32}, \qquad \text{(D.7)}$$

whose rank is four because $\rho_{i1} + \rho_{i2} = 1$, for $i = 1, 2, 3$. As a consequence, four additional equations are required, three of which are obtained by observing that the three second-order normalized cross moments $X_i X_j$ are zero, due to the linear transformation applied at the beginning of the procedure, and the fourth equation is obtained by writing the third-order moment $X_1 X_2 X_3$ in terms of the weights and abscissas, since its value is known. With the solution of the set of eight linear equations obtained above, the inversion algorithm is defined, and it is possible to compute the set of multi-variate weights and abscissas from the corresponding set of moments.

It is worth noting that all twenty moments considered in the third-order method, as well as the number of moments considered in the higher-order methods adopted in this work, are required to define the moment-inversion algorithm that allows the weights and abscissas to be computed. In the case of the third-order method:

• Ten pure moments in each spatial direction (M_{000}, M_{100}, M_{010}, M_{001}, M_{200}, M_{020}, M_{002}, M_{300}, M_{030}, M_{003}) are required to find the univariate weights ρ_{ij} and abscissas X_{ij}.

• Three second-order cross moments M_{110}, M_{101}, M_{011} and third-order cross moment M_{111} are used to obtain a linear system for the multivariate weights with a unique solution.

• The remaining six moments (M_{210}, M_{201}, M_{210}, M_{120}, M_{102}, M_{021} and M_{012}) are required to have closed expressions of the other third-order moments.

As a consequence, the set of moments required to define the quadrature approximation with two nodes for each spatial direction is exactly made of the twenty considered elements. Similar conclusions apply to higher-order methods [19].

References

[1] B. J. Adler, and T. E. Wainwright, Studies in molecular dynamics, II, behavior of small number of elastic spheres, J. Chem. Phys., 33 (1960), 2363–2382.

[2] A. E. Beylich, Solving the kinetic equation for all Knudsen numbers, Phys. Fluids., 12 (2000), 444–465.

[3] P. L. Bhatnagar, E. P. Gross, and M. Krook, A model for collisional processes in gases, I, small amplitude processes in charged and neutral one-component systems, Phys. Rev., 94 (1954), 511–525.

[4] G. A. Bird, Molecular Gas Dynamics and the Direct Simulation of Gas Flows, Oxford University Press, 1994.

[5] A. V. Bobylev, J. A. Carrillo, and I. M. Gamba, On some properties of kinetic and hydrodynamic equations for inelastic interactions, J. Stat. Phys., 98(3/4) (2000), 743–773.

[6] J. J. Brey, J. W. Dufty, C.-S. Kim, and A. Santos, Hydrodynamics for granular flow at low density, Phys. Rev. E., 58 (1998), 4638–4653.

[7] J. J. Brey, F. Moreno, and J. W. Dufty, Reply to "Comment on Model kinetic equation for low-density granular flow", Phys. Rev. E., 57(5) (1998), 6212–6213.

[8] J. J. Brey, M. J. Ruiz-Montero, and D. Cubero, Homogeneous cooling state of a low-density granular flow, Phys. Rev. E., 54 (1996), 3664–3671.

[9] N. F. Carnahan, and K. E. Starling, Equation of state for nonattracting rigid spheres, J. Chem. Phys., 51 (1969), 635–636.

[10] J. A. Carrillo, C. Cercignani, and I. M. Gamba, Steady states of a Boltzmann equation for driven granular media, Phys. Rev. E., 62(6) (2000), 7700–7707.

[11] J.A. Carrillo, A. Majorana, and F. Vecil, A semi-Lagrangian deterministic solver for the semiconductor Boltzmann-Poisson system, Commun. Comput. Phys., 2(5) (2007), 1027–1054.

[12] C. Cercignani, The Boltzmann Equation and Its Applications, Springer-Verlag, 1988.

[13] C. Cercignani, Rarefied Gas Dynamics, Cambridge University Press, 2000.

[14] S. Chapman, and T. G. Cowling, The Mathematical Theory of Non-Uniform Gases, Cambridge University Press, 2 edition, 1961.

[15] O. Desjardin, R. O. Fox, and P. Villedieu, A quadrature-based moment method for dilute fluid-particle flows, J. Comput. Phys., 227 (2008), 2524–2539.

[16] J. W. Dufty, A. Baskaran, and L. Zogaib, Gaussian kinetic model for granular gases, Phys. Rev. E., 69 (2004), 051301.

[17] J. H Ferziger, and M. Peric, Computational Methods for Fluid Dynamics, Springer, 2002.

[18] R. O. Fox, A quadrature based third-order moment method for dilute gas-particle flows, J. Comput. Phys., 227 (2008), 6313–6350.

[19] R. O. Fox, Higher-order quadrature-based moment methods for kinetic equations, J. Comput. Phys., 228 (2009), 7771–7791.

[20] R. O. Fox, Optimal moment sets for multivariate direct quadrature method of moments, Ind. Eng. Chem. Res., 48 (2009), 9686–9696.

[21] R. O. Fox, F. Laurent, and M. Massot, Numerical simulation of spray coalescence in an Eulerian framework: direct quadrature method of moments and multi-fluid method, J. Comput. Phys., 227(6) (2008), 3058–3088.

[22] R. O. Fox, and P. Vedula, Quadrature-based moment model for moderately dense polydisperse gas-particle flows, Ind. Eng. Chem. Res., 49(11) (2010), 5174–5187.

[23] J. E. Galvin, C. M. Hrenya, and R. D. Wildman, On the role of the Knudsen layer in rapid granular flows, J. Fluid. Mech., 585 (2007), 73–92.

[24] V. Garzo, and J. W. Dufty, Dense fluid transport for inelastic hard spheres, Phys. Rev. E., (59) (1999), 5895–5911.

[25] I. Goldhirsch, Rapid granular flows, Ann. Rev. Fluid. Mech., 35 (2003), 267–293.

[26] A. Goldshtein, and M. Shapiro, Mechanics of collisional motion of granular materials, I.

general hydrodynamic equations, J. Fluid. Mech., 282 (1995), 75–114.

[27] R. G. Gordon, Error bounds in equilibrium statistical mechanics, J. Math. Phys., 9 (1968), 655–662.

[28] L. H. Holway, New statistical models for kinetic theory, methods of construction, Phys. Fluids., 9(9) (1966), 1658–1673.

[29] J. T. Jenkins, Kinetic theory for nearly elastic spheres, In H. J. Hermann, J. P. Hovi, and S. Luding, editors, Physics of Dry Granular Media, Kluwer, 1998.

[30] J. T. Jenkins, and S. B. Savage, A theory for the rapid flow of identical, smooth, nearly elastic, spherical particles, J. Fluid. Mech., 130 (1983), 187–202.

[31] D. L. Marchisio, R. D. Vigil, and R. O. Fox, Quadrature method of moments for aggregation-breakage processes, J. Colloid. Interface. Sci., 258(2) (2003), 322–334.

[32] J. C. Maxwell, On stresses in rarefied gases arising from inequalities of temperature, Philos. Trans. R. Soc., 170 (1879), 231–256.

[33] R. McGraw, Description of aerosol dynamics by the quadrature method of moments, Aero. Sci. Technol., 27 (1997), 255–265.

[34] B. Perthame, Boltzmann type schemes for compressible Euler equations in one and two space dimensions, SIAM J. Numer. Anal., 29(1) (1990), 1–19.

[35] H. Struchtrup, Macroscopic Transport Equations for Rarefied Gas Flows, Springer, 2005.

[36] V. Vikas, Z. J. Wang, A. Passalacqua, and R. O. Fox, Development of high-order realizable finite-volume schemes for quadrature-based moment method, 4 January 2010.

[37] J. C. Wheeler, Modified moments and Gaussian quadratures, Rocky. Mount. J. Math., 4 (1974), 287–296.

[38] D. Wright, R. McGraw, and D. E. Rosner, Bivariate extension of the quadrature method of moments for modeling simultaneous coagulation and sintering particle populations, J. Colloid. Interface. Sci., 236(2) (2001), 242–251.

[39] C. Yuan, and R. O. Fox, Conditional quadrature method of moments for kinetic equations, J. Comput. Phys., submitted, 2010.